X-ray tomographic observations of microcracking patterns in fibre-reinforced mortar during tension stiffening tests

Nicolas Ducoulombier, Camille Chateau, Michel Bornert, Jean-François Caron, Patrick Aimedieu, Timm Weitkamp, Jonathan Perrin, Andrew L. King, Mario Scheel

X-RAY TOMOGRAPHIC OBSERVATIONS OF MICROCRACKING PATTERNS IN FIBRE-REINFORCED MORTAR DURING TENSION STIFFENING TESTS.

NICOLAS DUCOULOMBIER[*], CAMILLE CHATEAU[*], MICHEL BORNERT[*], JEAN-FRANÇOIS CARON[*], PATRICK AIMEDIEU[*], TIMM WEITKAMP[†], JONATHAN PERRIN[†], ANDREW KING[†] AND MARIO SCHEEL[†]

[*] **Laboratoire Navier, UMR 8205, CNRS, ENPC, IFSTTAR, Université Paris-Est, Marne-la-Vallée F-77455, France**

[†] **Synchrotron SOLEIL, St-Aubin 91192, France**

Abstract: For the last decades, new reparation or fabrication processes have been studied to replace traditional rebar by roving of different mineral or organic fibres to avoid corrosion issues. Such materials refer to the family of cementitious composite. Their tensile strength would directly depend on the proportion of reinforcement but also strongly on the interfacial mechanical properties between fibres and cementitious matrix. From now, evaluation of interfacial properties was mostly limited to the use of force-displacement curves obtained from mechanical experiments. This work presents a new methodology using micromechanical tension stiffening tests combined with X-ray computed tomography (XRCT) observations, performed at the Anatomix beamline at Synchrotron Soleil, and specific image processing procedures. Multi XRCT acquisitions with suitable scanning strategy are used to image the whole fibre-matrix interface along centimetric samples at four to five different levels of loading magnitude. Intensive image processing is then performed on tomographic images including digital volume correlation (DVC), image subtraction and Hessian-based filtering. This experiment allows to study damage mechanisms at small scale. The proposed methodology shows great potential to provide both qualitative and quantitative elements on interfacial mechanical behaviour such as crack growth and crack orientation. The interface between mortar and sufficiently small multi-fibre yarn used in this paper is shown to behave in certain condition as traditional rebar interface producing conical cracks in the surrounding matrix rather than debonding in mode 2, permitting a much higher energy dissipation during debonding. According to this study, conical cracks repartition and geometry are mostly influenced by the cementitious matrix. The spacing between cracks goes from 50 to 100 μm and the angle between crack normal vector and yarn orientation goes from 35 to 50 degrees.

Key words: Fibre-Reinforced Concrete, Interfacial Damage, Micromechanical Testing, X-ray Tomography

1 INTRODUCTION

Reforming concrete reinforcement strategies is a difficult task. Indeed, traditional reinforced shuttered concrete industry is well-organised, ultra-regulated and its mechanical efficiency has been well-proven since a century. Nevertheless, reinforced concrete structures may show poor durability due to corrosion of steel rebar, which can yield to dramatic collapse. Indeed, a large part of existing infrastructures worldwide becomes quite old and would need to be either reinforced or demolished and reconstructed to avoid other accidents. This aspect linked to reparation cost and resource shortage is a driving force pushing construction actors to develop new ways of reinforcing concrete either for construction or reparation purposes. Mineral and organic fibres are good candidates to replace steel rebar. The straightforward strategy is to manufacture rebar using those materials, for instance, composite rods from mineral fibres that can be used instead of steel [1] [2]. However, these rods are generally less stiff than steel rebar (if we omit those made of very expensive high modulus carbon fibres) and the obtained reinforced concretes are often less ductile than traditional steel reinforced ones. Another method would be to use short mineral fibre-reinforced concrete. Alkali-Resistant glass fibres (AR-GF) have been used for a long time to improve concrete properties, such as ductility [3] [4]. But their mostly isotropic orientation distribution in the mix, and the strong limitation on fibre amount (lower than 3%) due to the needed workability of the fresh mix, prevent it from using them to play the role of steel rebars [5]. A more recent methodology consists in using continuous fibres or filaments, which are tied together into yarns or rovings. Their very large slenderness makes their final orientation dependent on the concrete flow, which is not appropriate for traditional construction process. However, this property could become a benefit for new fabrication processes for which such reinforcements could be oriented in the desired direction. Textile reinforced concrete or mortar (TRC or TRM) are typical examples obtained using such roving in grid form for reinforcement of cementitious matrix. They have been developed to both build efficient lightweight structures [6]-[7] and to reinforce old buildings and infrastructures [8]-[9]. In addition, automation in construction is a formidable means of developing new efficient construction processes that make a full use of alternative reinforcement for concrete. In particular, this work is part of a larger project that aims to reinforce 3D printed concrete by integrating mineral fibre rovings during concrete extrusion to obtain unidirectional cementitious composites. It is worth noting that as diameter of the reinforcement is getting lower, the number of reinforcement elements per unit cross section, which is inversely proportional to the square of diameters, increases. Thus, using small mineral fibres remains an interesting issue, as the material can be seen as a composite material with a modification of bulk mechanical properties. At the same time, using more reinforcement elements in the same section decreases reinforcement spacing, what imposes to use finer cementitious matrix, i.e. finer aggregates.

Using roving of mineral or organic fibres as reinforcement of concrete is then promising, but an important amount of research is still needed to better understand both short and long-term mechanical behaviour of the different proposed processes resulting in a particular cementitious composite. Regarding brittle matrix composites, their mechanical properties would be governed by the relative amount of reinforcement with a given matrix, but they would also strongly depend on interfacial properties between matrix and roving. An additional difficulty comes from the fact that roving is an assembly of many micrometric filaments or fibres [10]. Indeed, in that case, damage behaviour at interface and stress redistribution in the roving are much more

difficult to characterize. Numerous studies have already been conducted on interface in cementitious composites. Nevertheless, the great variability and inhomogeneity in the cementitious matrix itself and the possible influence of the yarn on its compactness and composition strongly increase the variability of results. A standard method is based on comparisons between pull-out experimental force-relative displacement curves and simulations using a given model [11] [12] [13] [14] [15] [16] [17]. This methodology allows for the determination of respective interfacial parameters, usually fitting maximal pull-out force and residual frictional force, whenever non null. A recent review of pull-out tests is provided by Teklal et al.[18]. With multi-fibre yarns, impregnation by the cementitious matrix has been evidenced, from scanning electron microscopy (SEM) observations and mechanical tests, to constitute a key parameter [19] [20] influencing pull-out properties. Nevertheless, concerning direct observations, apart from specific considerations based on SEM analyses on the deterioration due to cement alkalinity of multi-fibre yarns [21] [22], no direct observation has been made on progressive damage that develops at the interface between yarn and cementitious matrix, up to the authors' knowledge. In the present study, an alternative micromechanical test, called "tension stiffening", is proposed to study interaction between cementitious matrix and yarn (see Ducoulombier et al.[23] for details). It consists in pulling on a single yarn locally embedded in the matrix on a ten to twenty mm-long area. It was inspired by the traditional macroscale "tension stiffening" test used for the determination of rebar/concrete interfacial properties [24]. It has been preferred over other existing micromechanical tests because of the simplicity of the loading conditions, its ability to provide in a single experiment two pull-out tests (one at both ends of the sample) and its additional ability to give access to residual frictional stress.

This work will precisely address that question of direct damage observation by a specific experimental tension stiffening set-up designed to be run within a high resolution X-ray computed tomography (XRCT) setup, namely that of the new Anatomix beamline of Synchrotron Soleil (Saint Aubin, France). This non-destructive imaging technique allows in situ experiments to be performed [25]. In addition, when associated with appropriate digital volume correlation (DVC) [26], image subtraction techniques [27] and hessian-based segmentation technique [28], it was shown to be efficient to detect tiny cracks in a lightweight cementitious material. In this paper, the same image processing is used for the analysis of several in situ tension stiffening tests. The methodology is shown to be powerful not only to give qualitative information on interfacial damage modes, but also to provide quantitative elements such as crack growth or crack orientation. Such elements can be of great interest to formulate or enhance assumptions underlying micromechanical modelling of the damage phenomena. Furthermore, when associated with the measurement of mesoscale force-displacement curves, they provide complementary information to quantitatively identify interfacial constitutive parameters.

After the first section, which deals with specimen specifications, experimental set-up and protocol, the second part of this paper describes the image processing and the resulting measurements, the accuracy of which is discussed. Then, specific observations of typical matrix/yarn couples are separately detailed. Finally, global geometrical information are obtained using hessian eigenvector analysis for each sample and are discussed.

2 EXPERIMENTAL SET-UP

In the present section, after a quick presentation of the specimen geometry, the mechanical properties of its components and the fabrication process, the specific set-up developed for in situ testing is carefully described together with the testing protocol. Then, a brief description of both material and controlling software of the XRCT setup of the Anatomix beamline is provided before detailing imaging settings that were used for the experiment.

2.1 - Specimen Specification and Fabrication

A specimen is made of a given yarn embedded on its central parts in a prismatic-cementitious matrix. Two printable ordinary Portland cement (OPC) mortars were used for the experiment. The first one, denominated NAV has been formulated at Laboratoire Navier and the second one is a commercial printable mortar of Lafarge called NAG3. NAV was intentionally formulated to present a lower yield stress than NAG3 when casting in the specimen mould in order to provide a better impregnation. These mortars were associated with two mineral multi-fibre yarns. One is a basalt fibre yarn (BF) from Isomatex S.A. and the other is an S-Glass fibre yarn (S-GF) from AGY (S type is a high performance alkali resistant glass fibre). As a reference, both mortars were also associated with a stainless steel single-fibre yarn (SSF) from Sadevinox. "Yarn" here can then refer either to single-fibre or multi-fibre yarns. Geometrical and mechanical parameters are gathered in Table 1. Five specimens of each type were elaborated by casting concrete using a syringe in a 3D printed mould with one yarn passing through each specimen as shown in Figure 1. The plastic filament used to 3D print the mould is a BVOH filament, which dissolves in water. Then, one day after casting the concrete, the filled mould was immersed in a basin of water where it would be dissolved and specimens would cure at the same time. After 7 days, specimens with a single yarn at the centre of the mortar section were obtained. Note also that after fabrication, non-embedded parts of multi-fibre yarns were impregnated with epoxy resin with a brush. This aimed at preventing their premature rupture, ensuring homogeneous loading state at the tip of embedded yarns. But, in the case of a poor impregnation of the yarn by the cementitious matrix, as observed in the S-GF+NAG3 specimen, the resin could have partially penetrated in the embedded part of the yarn, artificially increasing the impregnation level of the embedded fibre. In that case, a potential positive influence of epoxy penetration on the interfacial properties is suspected and will be discussed in the dedicated section 4.2.

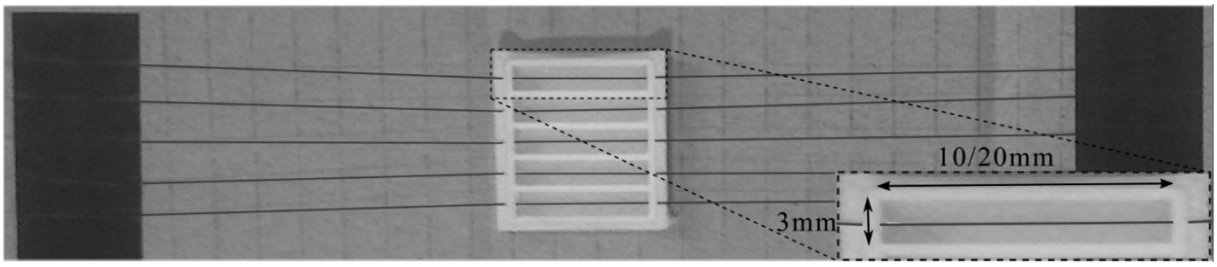

Figure 1: 3D printed mold with yarns before casting the printable mortar

2.2 Tension Stiffening Test

2.2.1 Macroscopic Results

As mentioned before, interaction between yarn and matrix are here studied through a so-called "tension stiffening" test. As illustrated in Figure 2, it consists in pulling on a single yarn locally embedded in the matrix on a ten to twenty mm-long area. The non-embedded parts of the yarn are called the "free areas".

Similarly to pull-out tests, each experiment provides a particular force-deformation curve. Figure 2 presents typical tension stiffening force-deformation curves of single-fibre yarn specimens on the left and multi-fibre yarn specimens on the right. Here, the deformation of the composite ε_c is calculated from the displacement u of extreme points A and B located on non-embedded parts of the yarn very close to the matrix as illustrated in Figure 2, i.e. $\varepsilon_c = (u_A - u_B)/\|AB\|_0$. The displacements were measured using digital image correlation as described in Ducoulombier et al.[23] In Figure 2, the obtained tension stiffening curves $F(\varepsilon_c)$ are associated with the force-deformation curves of free yarns $F(\varepsilon_f)$ for comparison, where ε_f is estimated from the displacement of points B and C similarly to ε_c. The various loading levels at which tomography investigations would be performed (see next section) are plotted on the same graph using punctual markers. Although these curves cannot provide direct identification of interfacial properties, they allow for comparisons between different types of yarns and matrix. Moreover, the macroscopic curves of the embedded yarns exhibit changes in the tangent stiffness, which suggests that damage events occur at microscopic scale. These events may result from three phenomena. The first damage mode is a progressive interfacial debonding between yarn and matrix, without external matrix cracking, which was expected and is suggested by the progressive slope change of the curves in Figure 2b. The second one is the yarn damage. It was however never observed on free yarns, which rather brutally break. The third one is the multi-cracking of the matrix, which was visually observed on the external surface of the specimen BF+NAG3 and S-GF+NAV3 and suggested by the jagged shapes of the last part of the curves in Figure 2c. However, during the experiment at Anatomix, all multi-fibre specimens' yarn breaks always occurred before significant multi-cracking of the matrix, at a rather low overall elongation. This observation might suggest that possible damage or deterioration of the yarns occurred due to X-rays radiation. But, during the experiment, no significant influence of X-rays radiation on the force or displacement data was observed. They remained stable all along the image acquisition. Besides, it is worth noting that the multi-cracking stage was observed on tests performed 3 months after the experiment at Anatomix with specimens of the same set. Consequently, these modifications seem to be rather linked with longer hydration period.

In this paper, only three different specimen would be deeply studied as an example to validate the interest of the proposed methodology. Further investigations would be the purpose of a future work.

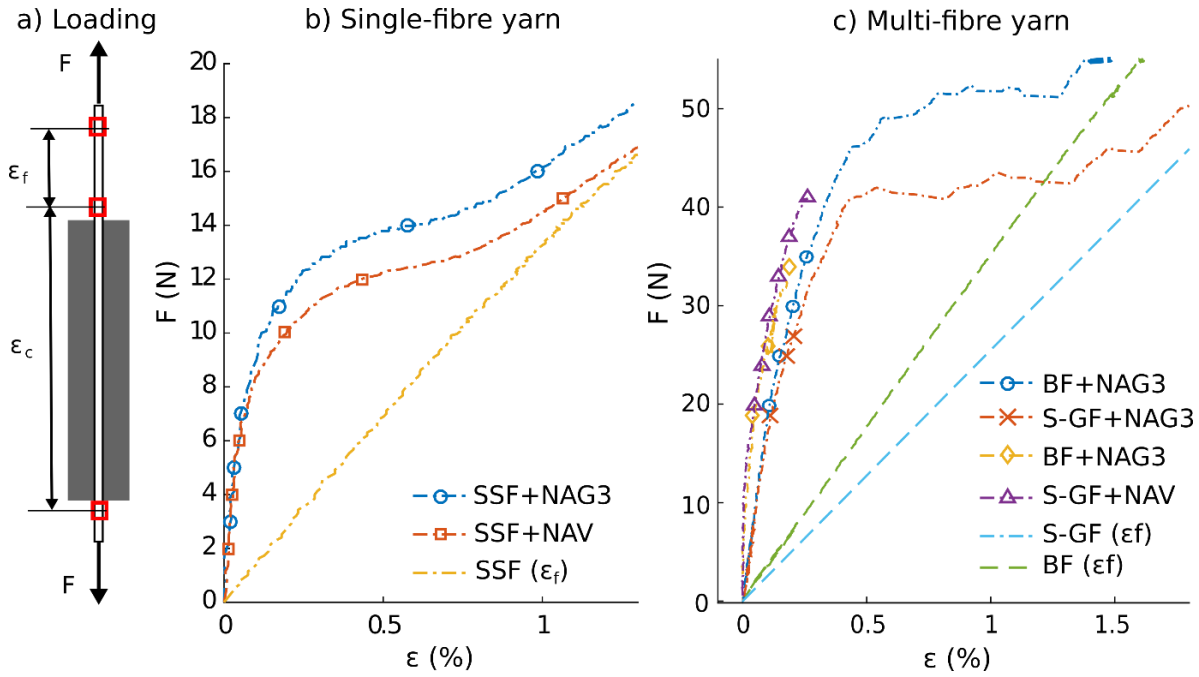

Figure 2: (a) Schematic loading conditions and (b, c) mesoscopic tension stiffening force-elongation curves with punctual markers indicating the levels of loading for tomographic investigations

2.2.2. In situ setup

In order to perform in situ tension stiffening tests, a specific mechanical frame was designed to fit on the XRCT setup of the Anatomix beamline. The latter essentially consists in a hollow air-bearing rotation stage (LAB Motion Systems, Heverlee, Belgium) with an internal diameter of 250 mm, associated with appropriate centring translation tables, and an indirect high-resolution image detector based on a single-crystal scintillator, visible-light microscope optics and a scientific-grade CMOS camera (details in following section). For an absorption-contrast experiment such as this one, the detector should ideally be placed close to the sample. As the overall force was quite low, we decided to take advantage of low-cost Fused Deposition Modelling (FDM) 3D printing technology to prototype the experimental frame. The scheme and a picture of the final design are shown in Figure 3. It integrates a LVDT displacement sensor (AMETEK OP1.5), which records the motion of a rigid loading beam, and a 30 N load sensor, which directly measures the load applied on the yarns. A specific acquisition device was programmed (LabView, National Instruments) to continuously record the actual loading, displacement and load/displacement curve. Furthermore, the yarn was only anchored by mechanical clamping using bolting. A constant-thickness load-bearing PMMA tube, almost transparent to X-rays, was used at specimen height to ensure no change in X-ray absorption during frame rotation and thus avoid image artefacts. The setup fits on a plate directly bolted onto the XY centring stage on top of the rotation stage of the tomography setup. The loading is manually applied by a micrometric screw that causes a displacement of the lower yarn anchorage by rotation of the loading beam as illustrated in Figure 3.

However, the load sensor capacity turned out to be too small for the multi-fibre yarn specimens. Therefore, when loading needed to be higher than the sensor capacity, the loading force was further evaluated by the measurement by DIC of the axial strain of the free area of the yarn whose stiffness was known precisely. To do so, an additional optical camera (AVT Pike 521) equipped with a Schneider Kreuznach 120mm-lens and appropriate extension tubes, fixed on

an independent tripod, was used. The free yarn was marked with black and white paint. The modified set-up is illustrated in pictures of Figure 3. This allowed increasing the loading up to 40 N for multi-fibre yarn specimens. Although that measurement was less accurate (in particular because of the unavoidable rotation of the yarn about its axis), it permits to estimate with an acceptable accuracy the relative increase of load between two successive tomography scans.

Mortar component	**NAV**	**NA G3**
CEM 1 (g)	600	/
Silica fume (g)	400	/
Quartz sand (g)	980	/
Total solid (g)	1980	2000
Water (g)	250	192
Superplasticizer (g)	9	9.2
Mechanical Properties		
Compressive Strength (MPa)	70	90
Young Modulus (GPa)	15±5%	20±5 %
Poisson ratio	0.21	0.21

Yarn properties	**S-GF**	**BF**	**SSF**
Fibre diameter (µm)	10	11	100
TEX (g/km)	150	100	62
Fibre count	≈350	≈400	1
Yarn section (0.01 mm²)	≈2.75	≈3.8	0.786
Yarn diameter (mm)	≈0.19	≈0.22	0.1
Mechanical Properties			
Traction Strength (N)	78±7 %	120±3 %	19.4± 0.5%
Associated stress strength (GPa)	2.84	3.16	2.5
Longitudinal Stiffness (N)	2550± 3%	3700± 3%	1374± 1%
Associated Young modulus (GPa)	81.8± 3%	97.4± 3%	175±1 %

Table 1: Mortars and yarns composition, geometrical and mechanical properties. Fibre traction Strength are the value obtained with specimen without mortar prism.

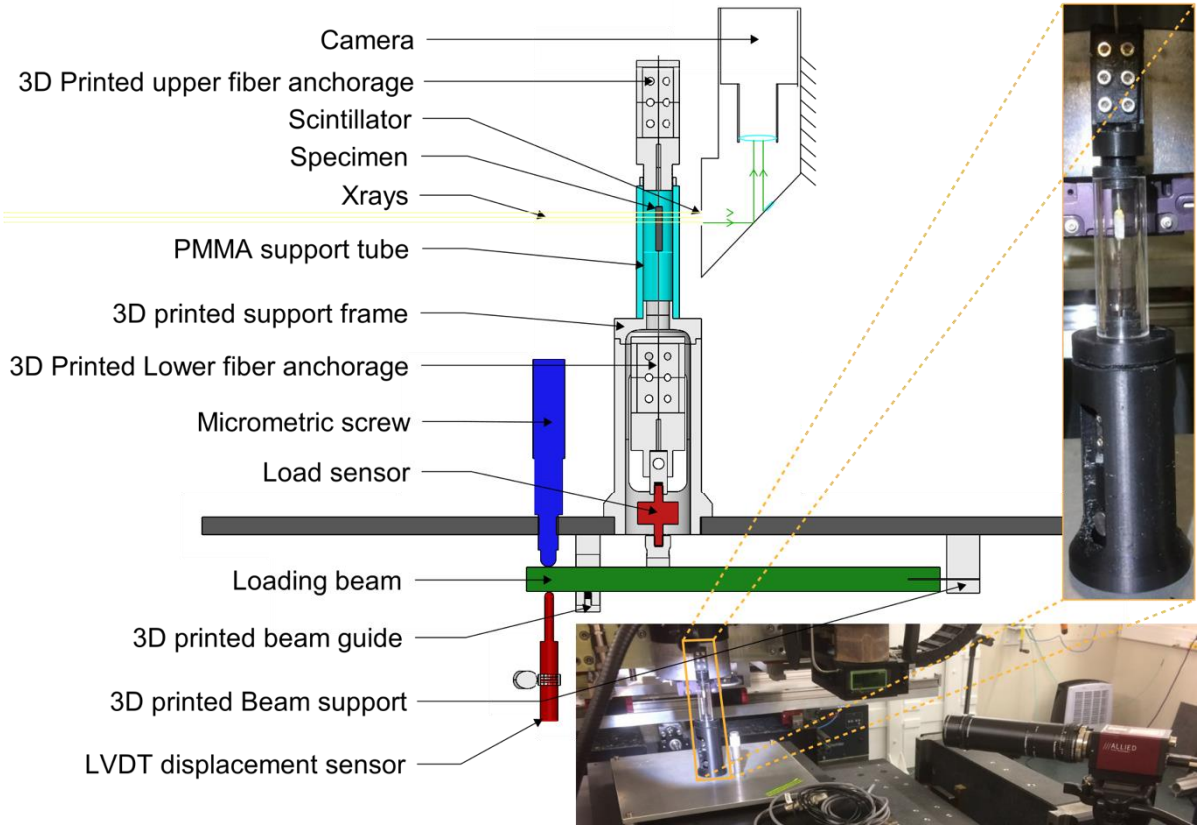

Figure 3: Scheme and pictures of the final design of the in situ tension stiffening frame

For each specimen, the experiment protocol sequence was defined as follows:

1) Specimen is mounted in the frame
2) The yarn is tightened using micrometric screw (and reference image for DIC are recorded whenever necessary)
3) Reference tomography scan is performed
4) Loading is increased until the first level of force is reached (with regular recording of images for DIC and associated evaluation of strain)
5) Wait for 15 min for the relaxation deformations to stabilise
6) New tomography scan is recorded
7) Repeat 4), 5) and 6) until yarn break

2.3– XRCT Imaging in Anatomix

Experiments were run on the recently established Anatomix ("Advanced Nanotomography and Imaging with coherent X rays") beamline of Soleil synchrotron facility [29] located in Gif-sur-Yvette, France, in the context of beamtime proposal no. 20181572. Anatomix is a 200-m-long beamline based on a cryogenic in-vacuum undulator (U18) and offers various tomographic setups for 3D imaging over a wide range of length scales, for various types of materials and using various contrasts. In the present study, a rather classical parallel-beam absorption tomography setup was used. The undulator was set with a gap of 5.5 mm and the beam was filtered by both an Au filter and Cu filter with appropriate thicknesses, resulting in a large-band pink beam centered at a photon energy around 38 keV. The X-ray radiographs were obtained with LuAG scintillator with adapted thickness mounted in front of a right-angle mirror, which redirects images to the CMOS sensor of an ORCA Flash 4.0 v2 camera from Hamamatsu, through either a 10x objective lens (numerical aperture NA = 0.28, working distance WD = 33.5 mm) or a 20x one (NA = 0.28, WD = 30.5 mm) from Mitutoyo and an adequate tube lens. The pixel size of the camera being 6.5 µm, this results in a voxel size of the reconstructed volumes of, respectively, 0.65 µm or 0.325 µm.

Typical acquisition includes the recording of a flat-field image for normalization before and after the scan, obtained by averaging 50 radiographs without sample, and a 180° scan of the sample containing 2000 projections (i.e., angle between projections was 0.09°). The scan duration was about 5 minutes for a pixel size of 0.65 µm and 10 minutes for pixel size of 0.325 µm. The acquisitions were made in continuous rotation mode using the FlyScan acquisition system [30] developed by SOLEIL. Every fifty scans or so, a background dark field without beam (to subtract the zero-intensity offset) was also recorded. All scanning information is summed up in table 2. As illustrated in Figure 4, various numbers of overlapping scans were necessary to cover the whole embedded yarn, depending on the specimen length and the magnification. Total duration to record the complete volume for each level of loading linearly depends on the number of scans. For small value of force, damage was supposed to be located near the embedded yarn ends and only partial acquisitions were made (see Figure 4). Note that in all cases, tomographic imaging was local, as the cross sections of the samples were larger than the detector field of view and the diameter of the reconstructed volume. Moreover, due to the long duration of a single acquisition, only one specimen of each type was tested in situ.

Radiographs were normalized using the corresponding dark and flat field images, and 3D images have been reconstructed from previously filtered projections using both ring filters and

Paganin filters [31] by means of the academic software PyHST2 [32]. Using these options with manually optimized parameters was efficient to significantly reduce ring and phase contrast artefacts.

Acquisition was controlled using the Spyc language, the SOLEIL Python command line interface, through a specific Python object developed by King et al[33]. It allows users to control in a unified interface both stage motions and image acquisition parameters, and thus to program procedures for the scanning sequence. In the present study, this feature was of great technical interest. The multiple acquisition procedure with 50 µm image overlaps required to record the whole interfacial area could be run in one single command using a specifically written Python script based on Spyc commands. For instance, the yarn centring, which can be quite time consuming, was made at both specimen ends only before launching the acquisition and was deduced by linear interpolation for all intermediate acquisitions.

	NAG3 + BF	NAG3+ S-GF	NAG3+ SSF	NAV+ BF	NAV+ S-GF	NAV+ SSF
Side length (mm)	~2.5	~2.5	~2.5	~2.5	~2.5	~2.5
Length (mm)	10	10	20	10	10	20
Voxel size (µm)	0.65	0.325	0.65	0.65	0.65	0.65
Number of acquisitions	10	17	17	8	9	17
Time per acquisition (min)	~5	~10	~5	~5	~5	~5
Total time for one loading (min)	50	170	80	40	45	40
Number of loading levels	6	4	5	4	6	5
Total beam time (min)	300	680	400	160	270	200

Table 2: General information on XRCT acquisition

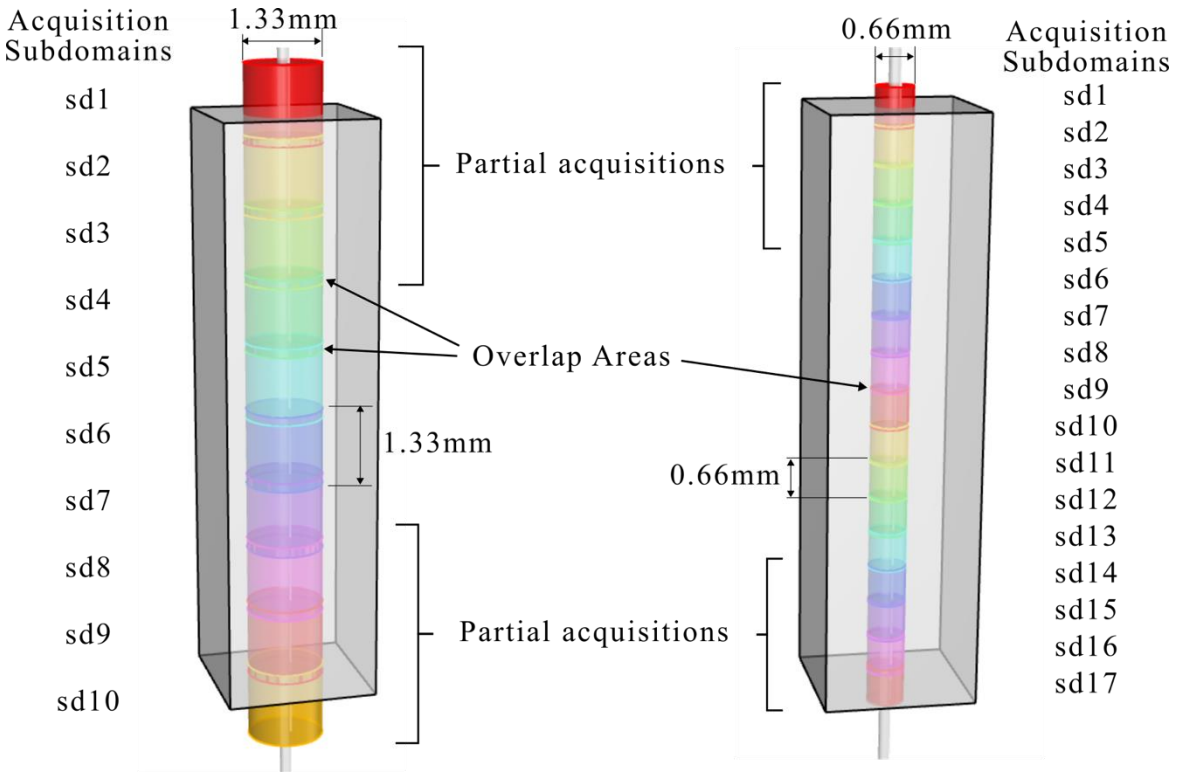

Figure 4: Schematic view of the XRCT acquisition procedure for a 10mm-long specimen with a voxel size equal to 0.65µm (BF+NAG3 and BF+NAV) on the left and 0.325 µm (S-GF+NAG3) on the right

3 – Image Processing Procedures

3.1- Image Compression

Images resulting from reconstruction are coded in 32-bit floating-point grey-level images. With a resolution of 2048^3 voxels, total memory size is then 32 gigabytes per image for one single acquisition. To save time and memory, the first operation was to rescale them to 8-bit integer grey-level images. It was performed to preserve a good balance between conservation of microstructural information and limited saturation of extreme values compared to 32-bit images. An example of typical grey level profile obtained with largest voxel size is plotted in Figure 5. Ordinary Portland cement (OPC) paste has a density close to quartz sand and a grey level around 70, porosity has a grey value around 30, basalt fibre around 85 and maximum density is reached in unhydrated OPC where grey level is 105.

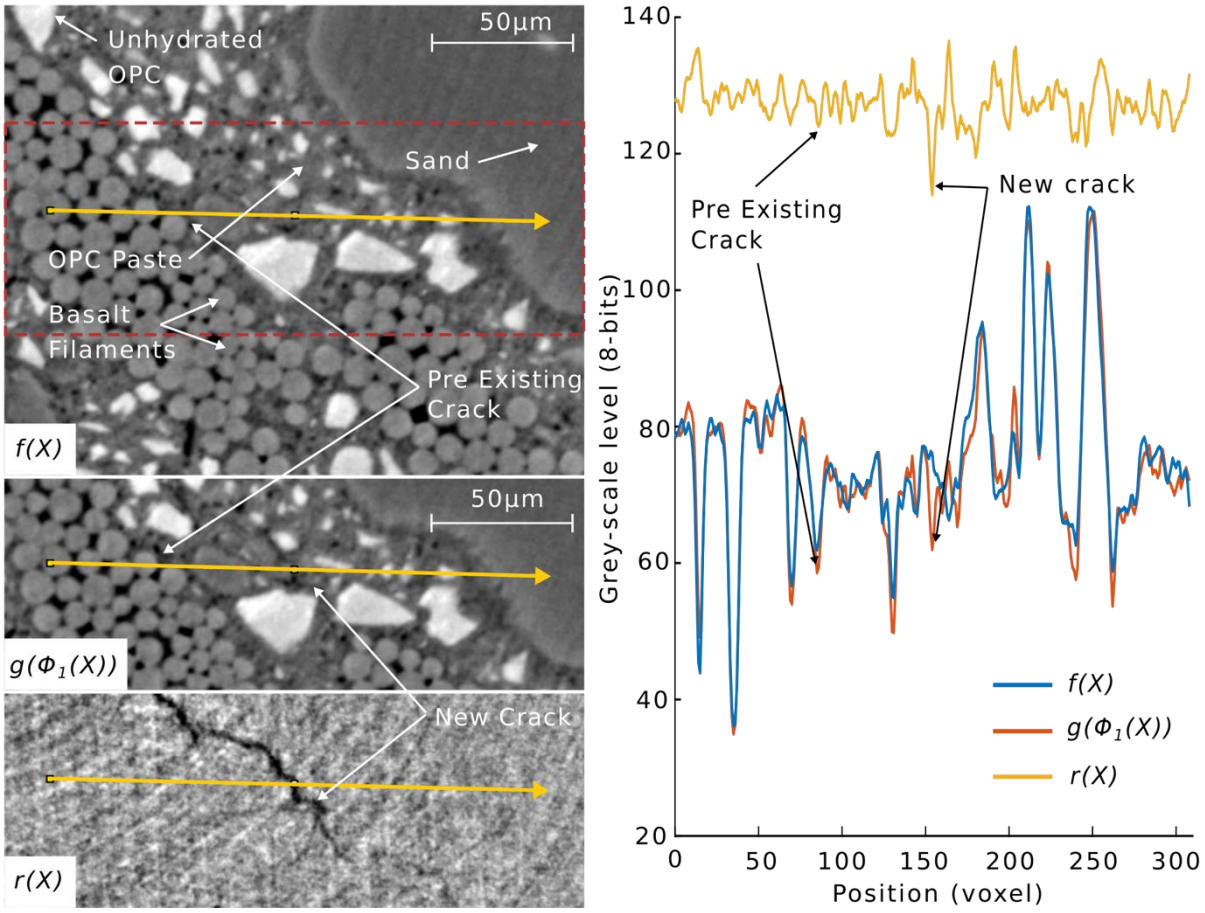

Figure 5: Typical 8-bit grey level XRCT image transversal slice of BF+NAG3 images and corresponding grey level profiles in different material phases: $f(X)$: Reference Image, $g(\phi_1(X))$: transformed image using best local transformation and $r(X)$: defined by equation (2) with k=128 (Contrast and brightness are adjusted to enhance visual aspect); yellow arrows indicate location of the respective grey-level profiles.

3.2- DVC

Digital Volume Correlation (DVC) analyses were performed on pairs of images, using the academic software CMV_3D developed at Laboratoire Navier [27],[34]. It consists in finding homologous positions of a set of material points in two images, considering the grey-level distribution in a small subvolume around each point [26]. As DVC principles can be found in existing literature [35],[36] as well as CMV_3D implementation details, only main features and used parameters are recalled here. The repartition of the correlation points is regular and forms a parallelepipedic grid. Spacing between points was chosen equal to the size of the correlation windows. The latter was determined from reference volume to include enough contrast in the cement paste, even in the larger OPC grains, what resulted in 30^3 voxels for 0.65µm voxel size and 50^3 pixels for 0.325µm voxel size. Each correlation point is located at the centre of its respective correlation window. Despite very small strain in concrete, a non-negligible rotation and translation of the specimen can occur during the test when load is applied. Therefore, the approximation ϕ_0 of the local mechanical transformation at the position $\boldsymbol{X}$, located in the neighbourhood of the position $\boldsymbol{X_0}$ of one correlation point in the reference image, has to take into account a rotation and a homogeneous deformation in addition to a simple rigid translation. Thus, it is defined as:

$$\phi_0(\boldsymbol{X}) = \boldsymbol{X}_0 + \boldsymbol{T}(\boldsymbol{X}_0) + \boldsymbol{F} \cdot (\boldsymbol{X} - \boldsymbol{X}_0), \qquad \text{for all } \boldsymbol{X} \text{ in } D \qquad (1)$$

where $\boldsymbol{T}$ is a pure translation, with 3 components to be evaluated, and $\boldsymbol{F}$ is the transformation gradient associated to an affine transformation. Here, the nine components of $\boldsymbol{F}$ are fixed and supposed to be equal to the overall deformation gradient (i.e. defined for the whole sample). It essentially captures the rigid motion between reference and loaded states. It needs to be estimated before the DVC algorithm is run and can be updated for a subsequent DVC calculation. In practice, the first estimation of $\boldsymbol{F}$ is made by matching by hand at least four non-coplanar points and using a standard least square fit. Thus, the correlation refers here to the minimisation of the so-called zero centred normalized cross-correlation coefficient (ZNCC), which leads to the determination of the three optimal components of the local translation $\boldsymbol{T}$ for all correlation points in the regular grid. This technique permits to decrease the complexity of the minimization, dividing by 4 the number of local transformation components (3 instead of 12) with no loss of accuracy with respect to the order of the assumed transformation, as the actual transformation is nearly a rigid motion (except for cracked areas). We refer to Bornert and al. [37] for a discussion on the links between order of the DIC shape function and measurement accuracy.

In practice, the optimisation of the local translation components is performed in two steps to increase the computational efficiency and robustness of the DVC routines. First, sets of discrete translations (i.e., with components equal to integer numbers of voxels) are systematically explored for the best correlation coefficient. Then, a new estimation of the global transformation gradient is calculated before subvoxel accuracy is searched by using an appropriate iterative continuous optimisation algorithm associated with an interpolation of the grey levels in the deformed image. DVC is computed only on correlation points that show enough local contrast and brightness, to insure that correlation provides physically meaningful position. In addition, optimisation is only performed for points at which the correlation coefficient obtained after the first step is below a user-selected threshold, fixed to 0.15 in the present study. It is recalled that ZNCC varies between 0 for perfect matching and 2 for perfect "opposite" contrast (never observed), with 1 corresponding to the absence of matching. This procedure might be iterated to check convergence but turns out to be very stable. Pairs of 3D 2048^3 voxels volumes, with about 300 000 correlation points, can be almost automatically processed this way, after a short manual pre-processing, in a couple of hours of computation on a standard workstation.

3.3- Image Subtraction

For brittle material with a rich microstructure such as concrete, image subtraction has been shown to be very efficient to detect tiny cracks[27]. Indeed, local modification of contrast due to cracks initiation and growth are difficult to discern from microstructure in XRCT image as illustrated in Figure 5. Perfect subtraction between cracked and reference images should permit to remove all the microstructure information that does not change after loading and then only highlight changes between both images, such as crack growth. Nevertheless, image noise and imaging artefacts would affect the quality of the subtraction result by creating artificial change between reference and cracked image. Specific artefacts that had occurred during XRCT imaging and their influence on image subtraction will be discussed below. The principle of image subtraction technique used in this article is explained in detail in a previous article [27]. It extends the concept of DVC residuals, which was already used in another context to quantify

cracks in heterogeneous materials [38], to local DVC and to images exhibiting domains with almost uniform grey levels. Only a quick overview, highlights on slight modifications and used parameters are mentioned here.

The subtracted image is defined in the reference configuration as:

$$r(\boldsymbol{X}) = g(\phi_1(\boldsymbol{X})) - f(\boldsymbol{X}) + k \quad (2)$$

where f, g and r stand for the grey levels in reference, deformed and subtracted images, respectively, and $\boldsymbol{X}$ is the location of a voxel in reference image. The voxel-wise transformation ϕ_0, determined by DVC in all correlation windows in which DVC was successful, is extended to every voxel by interpolating the transformation of nearby correlation points. The obtained local transformation ϕ_1 allows transforming the deformed image back to the frame of the reference image, which results in the so-called transformed image, by using a tricubic interpolation to compute the grey level $g(\phi_1(\boldsymbol{X}))$. Finally, the subtracted image is computed in 8-bit grey-scale using the offset value k set to 128 to ensure positive grey levels. Note that, because the imaging conditions remained stable, it was not necessary to account for global evolution of contrast and brightness between reference and deformed images. A distance criterion d is used to select the neighbour correlation points involved in the estimation of the local transformation ϕ_1. In the present paper, this parameter has been chosen equal to twice the spacing of the correlation grid. As mentioned in [27], the search of neighbour correlation points in a very large set can be really time consuming. Here, it was drastically reduced by taking advantage of the regularity of correlation points' grid: the search volume was reduced to a cube centred on the considered voxel with a side length of $2d$.

3.4- Discussion on crack detection performance

The methodology used to evaluate the performance of crack detection methodology is first introduced and illustrated in Figure 5 and Figure 6 on the BF+NAG3 specimen images (voxel size of 0.65µm). It is then applied on S-GF+NAG3 images, with a smaller voxel size (0.325 µm), leading to a discussion on the best choice for the voxel size.

As discussed by Chateau et al.[27], the image subtraction methodology is able to detect cracks with subvoxel opening and its performance is essentially controlled by the ratio of image noise level to the contrast between grey levels in solid phase and pores. It is thus of primary importance to evaluate these quantities.

A simple quantification of the image noise level in the reference image can be performed by considering grey level fluctuations in the sole sand particles, which can be supposed to be areas of almost uniform grey-level in an ideal noiseless image. As the grey levels in a noiseless subtracted image is expected to be fully uniform, apart from cracks, the fluctuation of any subdomain of the subtracted image can be considered. For the BF+NAG3 specimen, the image noise σ_f in the reference image is estimated using the single slice shown in Figure 6-a. It is defined as the standard deviation of the grey level values located in the areas circled in yellow, containing about 300 000 voxels, leading to $\sigma_f \leq 1{,}74$, where the inequality results from the possible physical variability of the sand particles X-Rays linear attenuation coefficient. The image noise σ_s in the subtracted image is estimated using the 3D cylindrical area delimited by the yellow circle in Figure 6-b and extending over a height of 200 slices, containing about 300 million voxels. It is equal to $\sigma_s = 2{,}49$. Note that noise in subtracted images can also be

calculated when considering the subtraction of the overlapping area of two neighbour 3D images of the reference stage (illustrated in Figure 4). It is thus estimated to 2.51, which shows that the loading of the sample does not influence the subtraction efficiency and that the possible presence of cracks does not significantly affect the grey level statistics.

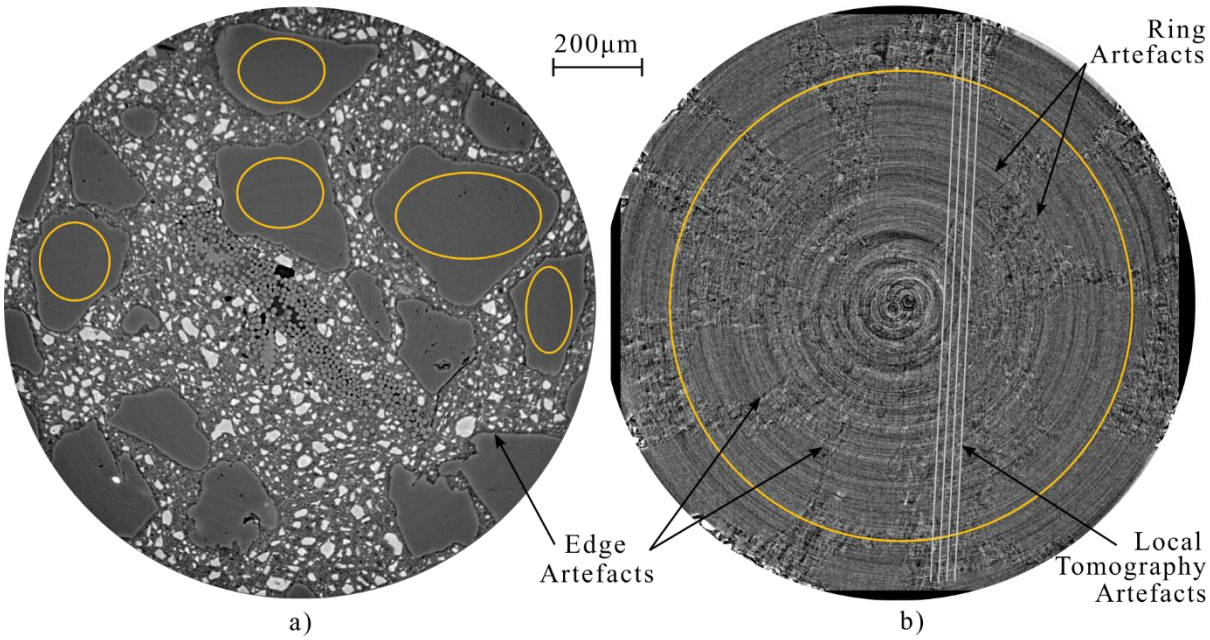

Figure 6: Examples of XRCT image transverse slices a) Reference image b) Subtracted image of the BF+NAG3 specimen; yellow lines delimit areas on which image noise is quantified; white lines emphasise local tomography artefacts

Besides, in perfect imaging condition, the only difference between two images of the same scene would be spatially and temporally uncorrelated random noise. Under such conditions, it can be demonstrated by statistical analysis that noise in the subtracted image is linked to noise in the reference image by the relation $\sigma_s = \sqrt{2}\sigma_f$. This theoretical relation is very closely verified by the above empirical noise standard deviation evaluations ($\sqrt{2}\ x\ 1.74 = 2.46$), which demonstrates the quality of the imaging system.

In addition to random noise, real XRCT images used in the present study show various artefacts, illustrated in Figure 6:

- The edge artefacts, i.e. wrong attenuation indications of X-rays near particle edges due to X-rays refraction, or so-called phase contrast, are observed even though the Paganin filter has been used to limit this effect.
- The ring patterns do not coincide in reference and loaded images and are thus still present in the subtracted images, in particular when they are close to phase opposition. They are clearly visible in the subtracted image in Figure 6-b. Some larger rings can also appear when some additional large dust particle pollutes the scintillator during the experiment. In this case, microstructure information of the corresponding toroidal area is lost.
- Subtracted images also show parallel lines patterns in one or more directions that spread over the whole sample, as highlighted in Figure 6-b by the set of white lines. In author's minds, these artefacts might be due to approximations induced by local tomography

performed on cubic specimen, i.e. with non-axisymmetric statistical repartition of density and X-rays absorption in the non-reconstructed part of the sample.

All these image artefacts and noises, which are barely visible in the images but are definitively present, are strongly emphasised by image subtraction and will limit the method's ability to detect crack occurrence and growth. In order to illustrate this fact, three corresponding transversal slices of the BF+NAG3 specimen in reference, transformed at last loading stage and subtracted images are shown in Figure 5. First, qualitative observations confirm the ability of the technique to remove all microstructural features on the subtracted image, including pre-existing cracks, and to enhance new cracks. Looking at the transformed image only, it would have been difficult, if not impossible, to notice the new crack and differentiate it from pre-existing ones. Once highlighted by the subtracted image, it is much simpler to detect and eventually segment the crack. In this particular case, the main new crack induces a local grey level variation much stronger than image artefacts (rings, lines and edges), which are also visible. Smaller crack like features are hard to separate from artefacts and noise.

Next, particular grey level profiles along lines located on these images are plotted in Figure 5. They illustrate in a quantitative way that the microstructure of mortar makes the crack detection a difficult problem. The subtracted profile shows that microstructure and pre-existing cracks are removed, while new cracks are highlighted.

Finally, following previous work [27], crack detection accuracy can be assessed by a quantification of the minimal crack opening e_{min} needed for detection, considering that the crack cannot be distinguished in the subtracted image if the induced grey-level drop δ is smaller than the standard deviation σ_s of the noise in the undamaged phase in the subtracted image:

$$\frac{\sigma_s}{\Delta_{max}} \leq e_{min} \leq \frac{2\,\sigma_s}{\Delta_{max}} \quad , \tag{3}$$

where e_{min} is the minimal opening expressed in voxels and Δ_{max} is the maximal grey level drop, which is calculated as the difference between the mean grey level in dense solid phase $\bar{g}_{sol}$ and the grey level in a porosity g_{por}. It is worth noting that in the worst case, grey level drop can be distributed over two neighbour voxels what explains the coefficient 2 in the upper bound of the above inequality. However, this simple accuracy assessment holds only for ideal imaging conditions such that actual spatial resolution of images coincides with the voxel size. In practice, the physical limitations of the imaging system or the subsequent image processing routines may induce a blur such that image spatial resolution might be significantly coarser than voxel size. Such a blur is characterised by its kernel or point spread function $K(y)$, which extends over a support larger than one voxel. The grey level drop induced by a crack would then not be localized on one or two pixels, but rather distributed over a window of pixels according to $K(y)$. A curious reader can refer to [39] for more specific information.

On the first hand, for the BF+NAG3 specimen (Figure 5, voxel size of 0.65µm), mean grey level in cement paste is equal to $\bar{g}_{sol} = 70$, and grey level in porosity is equal to $\bar{g}_{por} = 40$. Using equation (3) and the above evaluated standard deviation of grey level in the subtracted image, the minimal crack opening that would be detected in ideal conditions is then estimated as $0.08 \leq e_{min} \leq 0.16$ voxels, which corresponds to $0.05\ \mu m \leq e_{min} \leq 0.11$ µm (voxel size of 0.65 µm). However, due to the spatial resolution limitation induced by imaging conditions (sample to scintillator distance, scintillator thickness, numerical aperture of lens) and reconstruction algorithm (in particular ring artefact correction and Paganin filter), equation (3)

needs to be corrected for estimating of the crack thickness using the procedure described in [39], based on the integration of the grey levels in the subtracted image along a path normal to the crack surface. Looking at the graph in Figure 8, the maximal grey level drop in the above example is found to be close to 15 (to be compared to $\bar{g}_{sol} - \bar{g}_{por} = 30$), but spreads over several voxels, which suggests a crack opening of the order of one voxel.

On the other hand, images with the smallest voxel size 0.325 µm (S-GF+NAG3 specimen) offer twice the magnification (though not twice the spatial resolution) at the cost of a field of view half the size, with a total size of 0.66mm as illustrated in the schematic view in Figure 4. The subtracted image between reference and last loading stage obtained with this higher magnification shows a lower signal to noise ratio, with a standard deviation of noise between 7 to 10 and a maximal grey-level drop induced by cracks in deformed images equal to $\Delta_{max} = \mathbf{80}$. In such conditions, the use of equation (3) indicates that the smallest detectable crack aperture $\mathbf{e}_{min}$ is between 7/80 = 0.09 voxel and 10*2/80 = 0.25 voxel in the worst-case scenario, i.e. $\mathbf{0.03} < \mathbf{e}_{min} < \mathbf{0.08}$ µ**m**, assuming an ideal imaging setup.

Moreover, at that magnification, we observe the presence of a new kind of artefact that distorts the particles shape in the XRCT images. This is highlighted at the top of Figure 11 (zoom in the transversal cut of the transformed image at the last loading stage) where the GF filaments cross-sections do not look round. This distortion is supposed to be due to deformation associated with relaxation. Indeed, to obtain the same signal to noise ratio in the 3D images, a longer acquisition time is needed, so that delayed deformation has more time to develop during the scans. Moreover, the same displacement amount appears larger in images at higher magnification. In order to be less sensitive to the local distortion induced by relaxation and to embed enough contrast, the size of correlation window has been increased to 50 voxels. Taking into account the actual conditions inducing a spatial resolution coarser than the voxel size, the actual detection would be less accurate, but in any case somewhat more efficient than with the optical conditions used for the lower magnification. The use of a smaller pixel size might thus permit to enhance the crack detection, though not by the same factor than voxel size decrease, but a particular care needs to be taken with respect to relaxation for in situ experiments. When relaxation displacement is important, a lower magnification could be the better choice, providing an optimal trade-off between crack detection and size of field of view.

3.5- Hessian based segmentation and measurement of cracks orientation.

At this point, the method permits to detect cracks and to qualitatively discuss general damage patterns and their evolutions with loading. It should however be noticed that using the obtained subtracted image for the purpose of cracks segmentation would be rather difficult. Indeed, the particular case presented in Figure 5 shows that the segmentation using a simple thresholding method would probably yield to either loss of tiny cracks or include many voxels that do not belong to a crack. A more sophisticated solution to differentiate cracks from noise and acquisition artefacts such as rings, also proposed in [27], is the use of geometric information of the local grey-level drop provided by the comparison of eigenvalues $\lambda_3 \geq \lambda_2 \geq \lambda_1$ of the local hessian matrix, i.e. the second derivative of the grey-level in the subtracted image. Indeed, a crack is essentially a dark planar geometry, characterised by a local grey level drop following a particular direction, which is indicated by a large absolute difference between the higher eigenvalue and the two others. Therefore, the quantity $A(\boldsymbol{X})$, called "crackness" image, proposed in [28] and defined by equation (4), is a suitable quantity to evaluate the presence of a crack at a given position $\boldsymbol{X}$.

$$A(\boldsymbol{X}) = \lambda_3(\boldsymbol{X}) - |\lambda_2(\boldsymbol{X})| - |\lambda_1(\boldsymbol{X})| \quad (4)$$

The crackness has then been used to compute the binary image of detected cracks by a thresholding followed by the removal of smaller particles. The grey level threshold value was determined by hand and only particles larger than 300 voxels were retained. On various figures of next section, respective binary image of cracks is superimposed in yellow on the transformed images. Obtained images would be called "crack+transformed images". If this method showed a real practical interest, it should be however noticed that so far no quantitative element is given on the potential improvement of crack detection.

Finally, a broader use of the image hessian matrix is proposed in the present paper to analyse the mean crack orientation with respect to the yarn central axis. Indeed, the eigenvector $\boldsymbol{v_3}(\boldsymbol{X})$ associated with the larger eigenvalue $\lambda_3(\boldsymbol{X})$ is an estimate of the normal vector of the crack local orientation $\boldsymbol{n}(\boldsymbol{X})$ [28]. Then, the crack orientation map coded as a 16-bit RGB colour image is defined as follow:

$$\forall \boldsymbol{X}, \begin{cases} \boldsymbol{n}(\boldsymbol{X}) = \boldsymbol{v_3}(\boldsymbol{X}) \ , & A(\boldsymbol{X}) \geq A_{min} \\ \boldsymbol{n}(\boldsymbol{X}) = [0,0,0] \ , & A(\boldsymbol{X}) < A_{min} \end{cases} \tag{5}$$

Eventually, the orientation map is smoothed, by convolution with a uniform kernel, and re-normalized to remove irrelevant local fluctuations. This map provides rich quantitative information. In the present study, for each studied case, the crack orientation will be characterised by the statistical distribution of inclinations of cracks' normal vector with respect to the fibre direction (which in practice is along the z direction), noted $\varphi = \arccos(\boldsymbol{n} \,.\, \boldsymbol{e_z})$; and the deviation angle of its transversal component $\boldsymbol{n_t}$ with respect to $\boldsymbol{e_r}$, noted $\theta_d = \arcsin\left(\frac{\boldsymbol{n_t}}{\|\boldsymbol{n_t}\|} . \boldsymbol{e_\theta}\right)$. $\{\boldsymbol{e_r}, \boldsymbol{e_\theta}, \boldsymbol{e_z}\}$ are the unit vectors of the cylindrical coordinate system centred in the yarn central axis. Geometrical illustration of those specific angles is provided in Figure 7. From these distributions, many geometrical information can be computed. For instance, we propose in section 4.5 to estimate the representative crack geometry, based on an assumption about its geometry made from the observation.

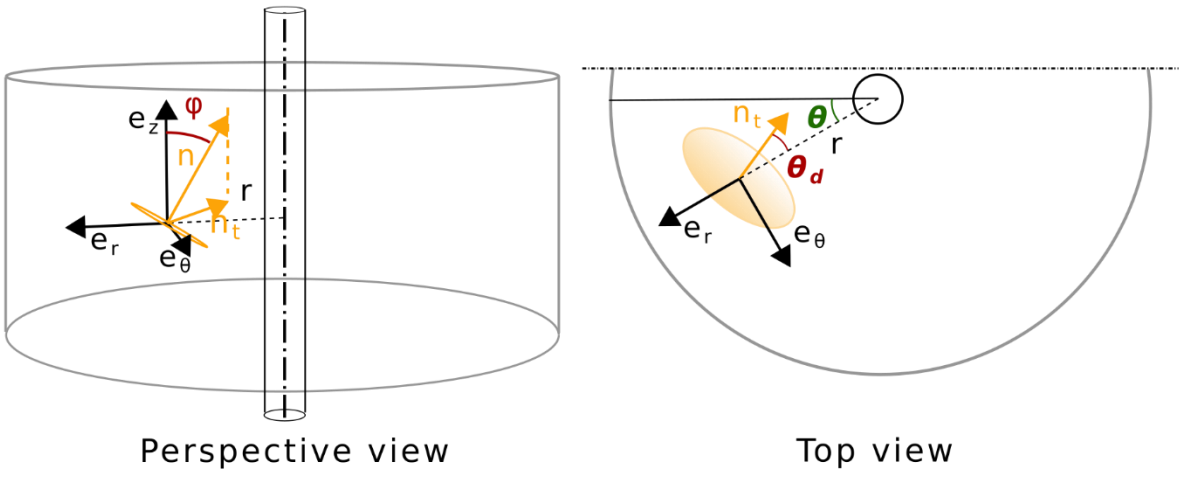

Figure 7: Definition of characteristic local angles of a crack in the cylindrical coordinate system

4 Interfacial damage of various single yarns embedded in mortar systems

This section describes the main observations of interfacial behaviour for various yarn/mortar couples. The combination of XRCT imaging of loaded specimens with the image subtraction technique allows for determining damage patterns and cracks' geometry as well as their

evolution with increasing load. All general results on damage mode, geometry and failure load for each specimen are gathered in Table 3. It indicates that the yarn type and the shape of its cross section primarily influence the interfacial bond, which is associated with a particular type of damage. In this part, the discussion is focused on the most interesting examples and the influence of these parameters on interfacial behaviour and damage pattern is carefully highlighted.

4.1 Basalt multi-fibre yarn (BF) embedded in NAG3 matrix

4.1.1 Geometry of interfacial debonding along the yarn

In this system, interfacial damage is characterised by the presence of pseudo periodic series of conical cracks in the surrounding matrix around the yarn. As illustrated in Figure 8, they are emitted from the yarn interface and they develop in the surrounding matrix towards the tip of the matrix cylinder. The detailed shape of those conical cracks is also affected by the matrix microstructure. Indeed, particles of sand tend to deviate the crack propagation. In addition, the crack transversal cross-section is similar in shape to the yarn cross-section. This damage pattern, with a network of cracks in the matrix rather than a single one along the yarn/matrix interface, testifies a strong bond between the yarn and matrix. It is also very similar to internal cracking pattern that develops at concrete-rebar interface near rebar ribs [24]. Another interesting feature is the dense transversal multi-cracking that develops between main part of the multi-fibre basalt yarn and a smaller portion of fibre separated from the main yarn in subdomain sd2 at the top of Figure 8. In that case, the damage pattern is similar to that of brittle matrix unidirectional composite, which is another proof of the good interfacial bond between multi-fibre yarn and matrix. Nevertheless, in the same sample, one may also find some local splitting debonding between yarn and matrix, which reflects a weaker bond between yarn and matrix. In particular, the bottom of Figure 8 illustrates a situation with a mixed damage mode, with one side of the interface splitting and the other emitting cracks in the surrounding matrix. For both conical and transversal cracks, the spacing is about 100µm.

Specimen		Impre-gnation	Yarn cross-section shape	Damage mode	Cracks shape in matrix	F_{max} (N)
BF+NAG 3	top	+	Flattened	Matrix cracking	Flattened Conical	40
	bottom	+		Mixed mode	Flattened Conical	
S-GF+NAG 3	top	- *	Round	Matrix cracking	Conical	32
	bottom	- *		Splitting	/	
BF+NAV	top	++	Rather round	Matrix cracking	Conical	35
	bottom	++		Matrix cracking	Conical	
S-GF+NAV	top	++	Round	Matrix cracking	Conical	36
	bottom	++		Matrix cracking	Conical	
SSF+NAG3	top	/	Round	Splitting	/	19
	bottom	/		Splitting	/	
SSF+NAV	top	/	Round	Splitting	/	19
	bottom	/		Splitting	/	

Table 3: Collection of experimental results: impregnation is sorted from "–", the lowest rate where most filaments are left un-impregnated to "++" for which most filament are impregnated by mortar. The "*" is added to mention that epoxy resin penetrates in the un-impregnated filament.

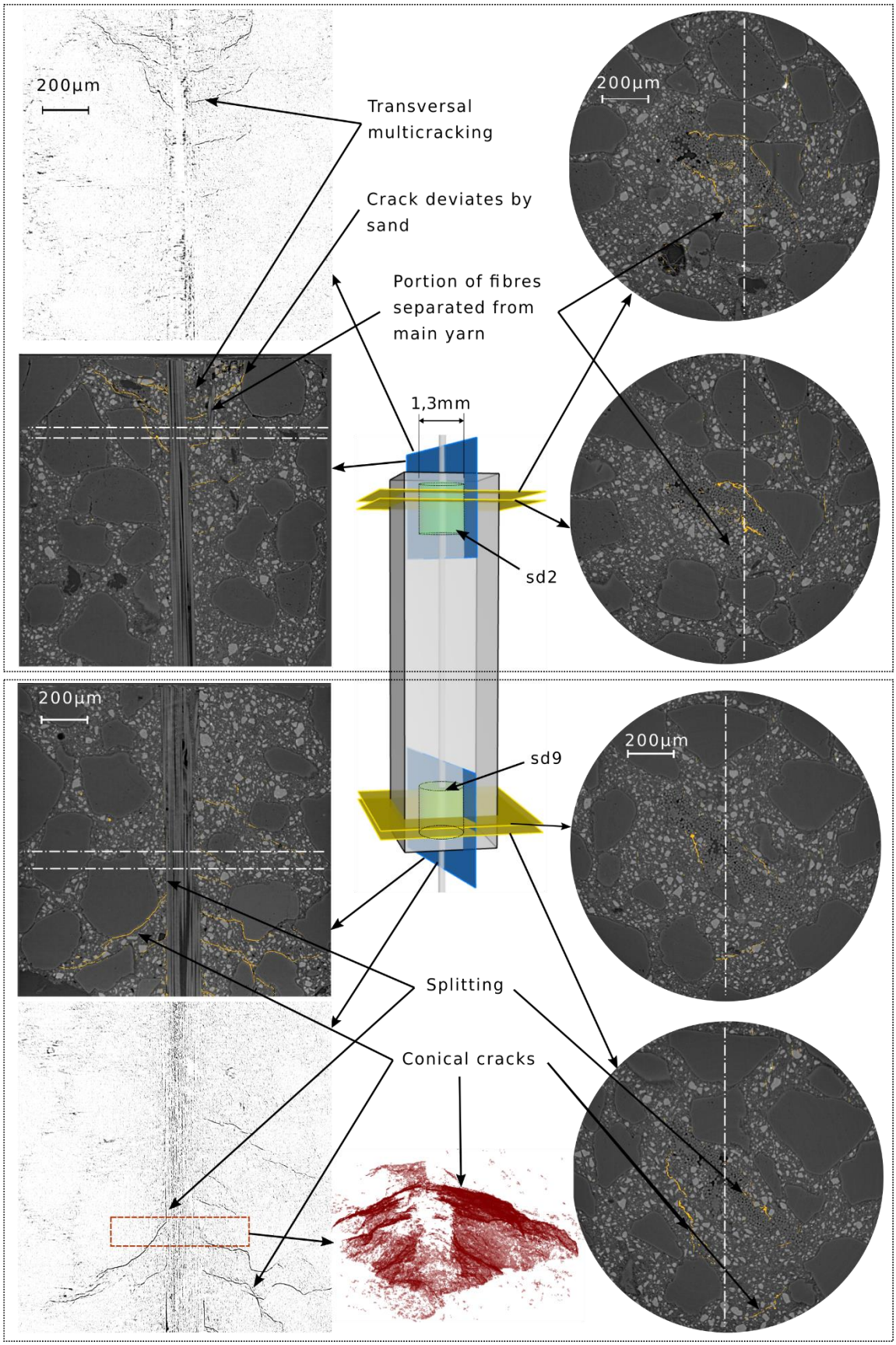

Figure 8: Geometry of debonding in the BF+NAG3 sample at the last loading stage. For both subdomains sd2 and sd9 (defined in Figure 4), a longitudinal slice, represented in both crack+transformed and crackness images on the left, is associated with two transversal slices of the

crack+transformed image on the right. A 3D rendering, highlighting the conical shape of the cracks, is also provided for subdomain sd9. These slices are defined on the schematic 3D view by yellow and blue planes respectively. The green cylinder represents the field of view of the local tomography. Voxel size is 0,65µm.

4.1.2 Debonding versus increasing loading

Figure 9 shows interfacial cracks evolution on transformed images of subdomains sd9 (defined in Figure 4) at several stages of increasing loads. For each loading stage, the position of the last crack emitted from the yarn can be identified. Defining the "debonded length" as the position along the yarn of the last emitted crack with respect to the mortar tip, one can follow its evolution with increasing load, as emphasised with red lines in Figure 9. From this identification, the force-debonded length curves for both ends of the sample are plotted in Figure 10. Both curves appear to be very similar, which shows that the symmetry of the mechanical problem is preserved during the whole experiment. The evolution of the debonded length with increasing load is found to be affine.

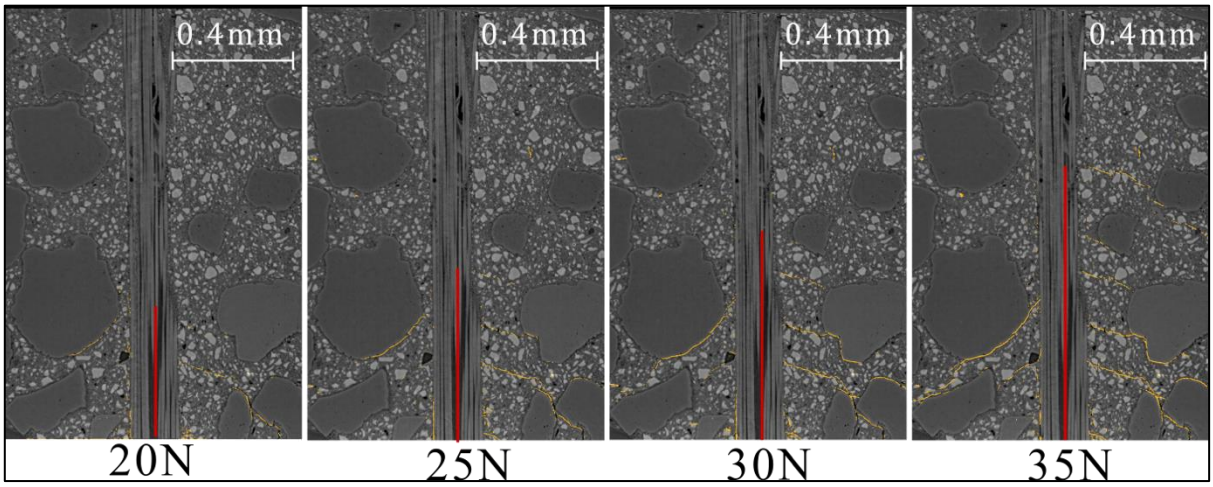

Figure 9: XRCT longitudinal slice of BF+NAG3 system showing evolution of debonded length (red line) and crack growth from crack+transformed images images of subdomain sd9 at various loading stage.

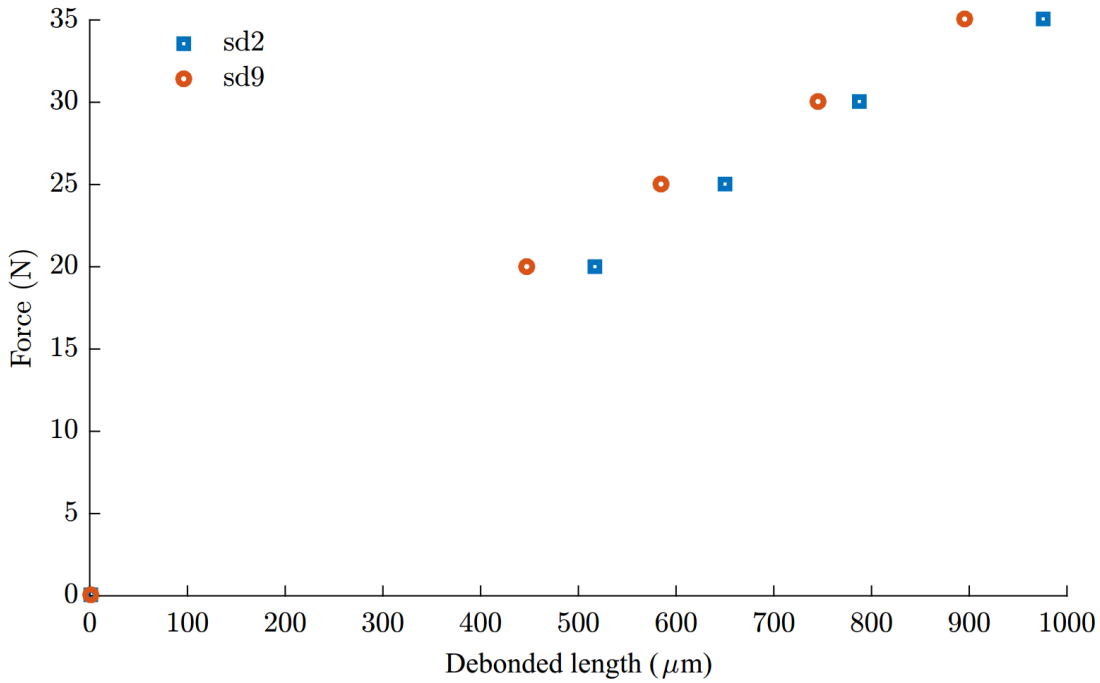

Figure 10: Evolution of debonded length versus applied force in BF+NAG3 at both ends of the specimen (subdomain sd2 and sd9 are defined in Figure 4).

4.2 Glass (S-GF) yarn embedded in NAG3 matrix

4.2.1 Geometry of interfacial debonding along the yarn

Two different damage patterns appeared at both sides of the specimen. They are illustrated in Figure 11. The first one, visible at the upper end (sd2) shows conical cracks emitted from the yarn that grow in the surrounding matrix, similar to those observed in the BF+NAG3 specimen. However, despite the deviation of some cracks by sand grains, cracks form more regular cones with rather circular transversal cross-sections, and almost no splitting is observed, as illustrated at the top of Figure 11. It is worth noting that at that tip, it seems that a substantial amount of epoxy resin penetrated through the non-impregnated yarn.

The opposite end of the specimen (sd16), illustrated at the bottom of Figure 11, shows a very different damage mode. Although a few small conical cracks are observed, yarn debonding occurs mostly by splitting between yarn and matrix. One can also observe some epoxy resin that penetrated through the non-impregnated filaments. More precisely, the splitting occurs between non-impregnated GF filaments and filaments impregnated in mortar, as shown in the zoom in transversal slice of the transformed image at the bottom of Figure 11.

To sum up, both ends of the specimen exhibit a significantly different behaviour, with a relatively low bond between yarn and matrix at the bottom (sd16-15-14-13), which induced splitting, and a better bond at the top (sd2) which induced a regular network of matrix cracks. At this point, the reasons for these opposite behaviours are still difficult to clarify, but the authors suspect that artificial improvement of impregnation is induced by the penetration of epoxy resin. The unequal repartition between both subdomains may explain the difference between respective damage patterns.

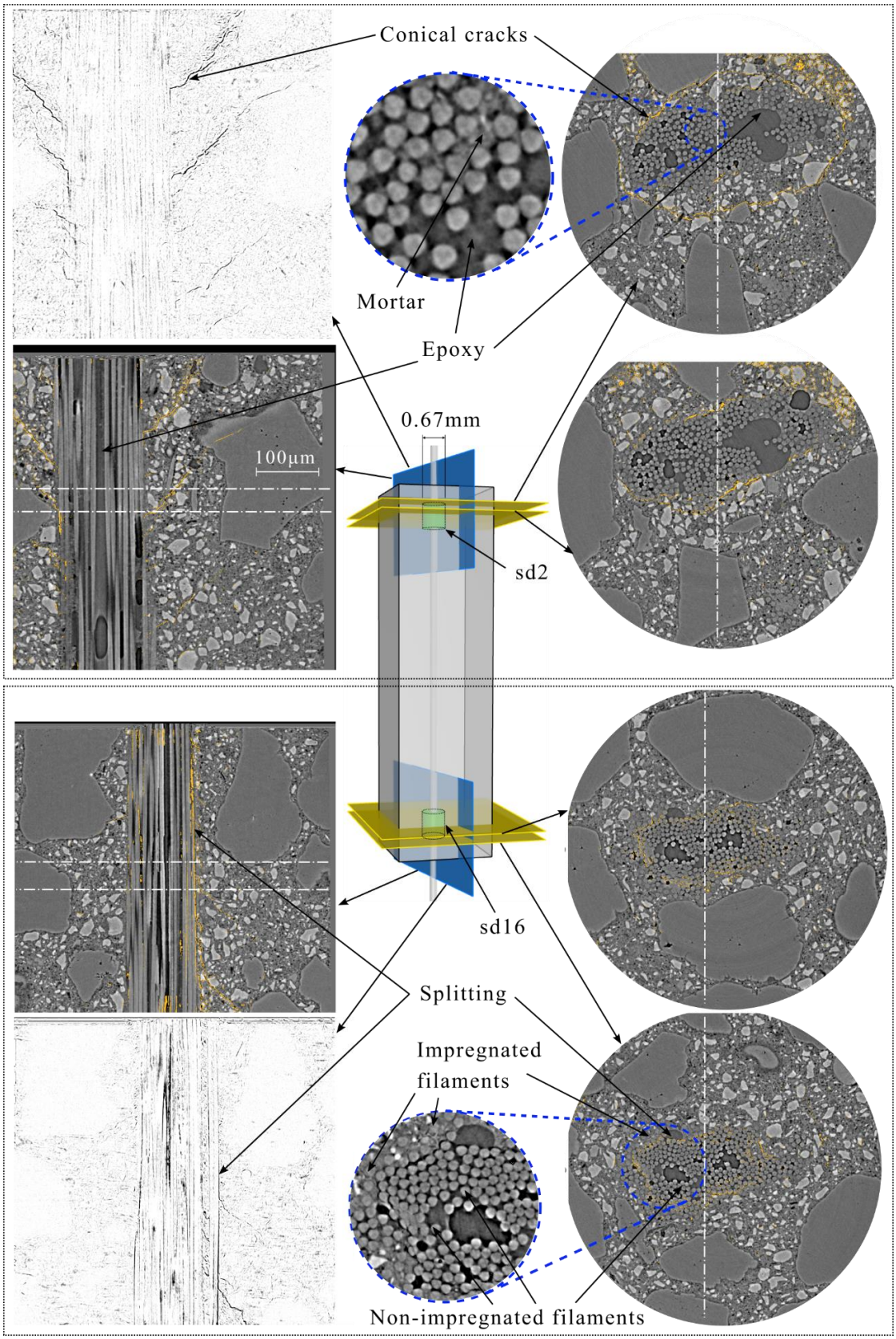

Figure 11: Geometry of debonding in the S-GF+NAG3 sample at the last loading stage, in the sd2 (top) and sd16 (bottom) sub-domains. The same longitudinal slice represented in crack+transformed and crackness image (left) is associated with two transversal slices of the crack+transformed image (right) that are defined in the central schematic 3D view by blue and yellow planes respectively. The green cylinder represents the field of view of the local tomography (voxel size is 0.325µm)

4.2.2 Evolution with increasing loading

Similarly to the BF+NAG3 specimen (section 4.1.2), the debonded length is estimated at both ends of the specimen for each applied load. Obtained debonded lengths are then plotted as a function of load in Figure 12. These curves show that at the end where debonding mostly happens by splitting, the debonded length for a same applied force is approximately twice the length of the other side where matrix cracking occurs. As expected, splitting occurs at a lower level of shear stress than matrix cracking. The symmetry of the mechanical problem is therefore lost during increasing loading.

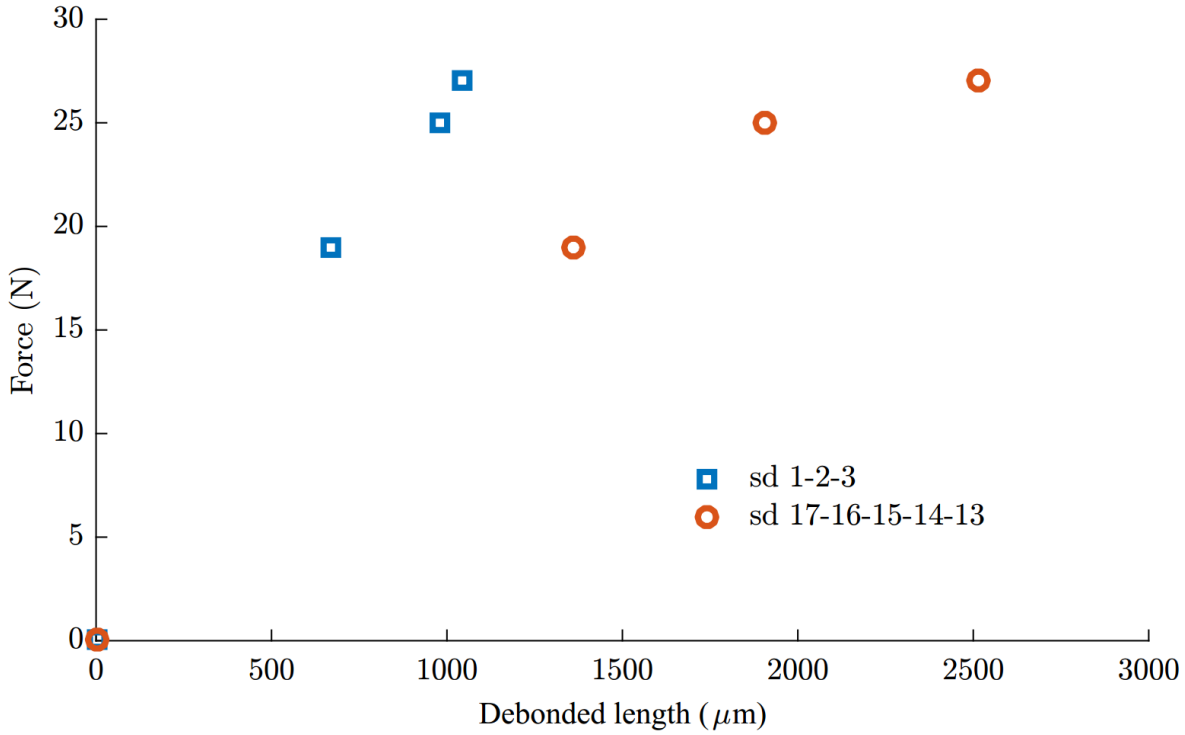

Figure 12: Yarn debonded length versus applied force at both ends of the S-GF+NAG3 sample, showing splitting in subdomains sd13-14-15-16-17 and matrix cracking in subdomains sd1-2-3. Subdomains are defined in Figure 4.

4.3 Basalt (BF) yarn embedded in NAV matrix

In existing literature [20], impregnation is identified to have a great impact on interface bond. To study this effect more in detail, the two mortars used in this study presented different rheological behaviour at early age. As stated in section 2.1, NAV was formulated with a smaller yield stress than NAG3 to improve impregnation. As expected and illustrated by the comparison between the BF+NAV transversal slice on the left of Figure 13 and the transversal slice of S-GF+NAG3 on the right bottom corner of Figure 11, the impregnation of BF+NAV is qualitatively better. In fact, the NAG3 mortar flew only through a small peripheral skin of the S-GF yarn, with a thickness of a few tens of micrometres, while the NAV mortar was able to penetrate deeply in the BF yarn over hundreds of micrometres. However, the NAV mortar that actually flew through the BF yarn shows more porosity than in the bulk and is only composed of the finer elements of the paste. Besides, both NAV and NAG3 mortars produced ettringite needles in the yarns porosity.

As for the other multifilament samples, the interfacial damage pattern in the BF+NAV sample (Figure 13) is composed of conical cracks emitted by the matrix which develop in the surrounding matrix. Their transversal cut seems again similar to the yarn cross-section. It is also worth emphasizing the dense transverse multi-cracking that occurs in the matrix that penetrated into the yarn, illustrated by the zoom made in the transversal slice on Figure 13-b. This damage pattern is also similar to those observed in other brittle matrix composite [4][40] and is the sign of a great interfacial bond and a good penetration of the matrix inside the yarn. The spacing is here smaller than the one observed in BF+NAG3 sample and equals to about 50µm.

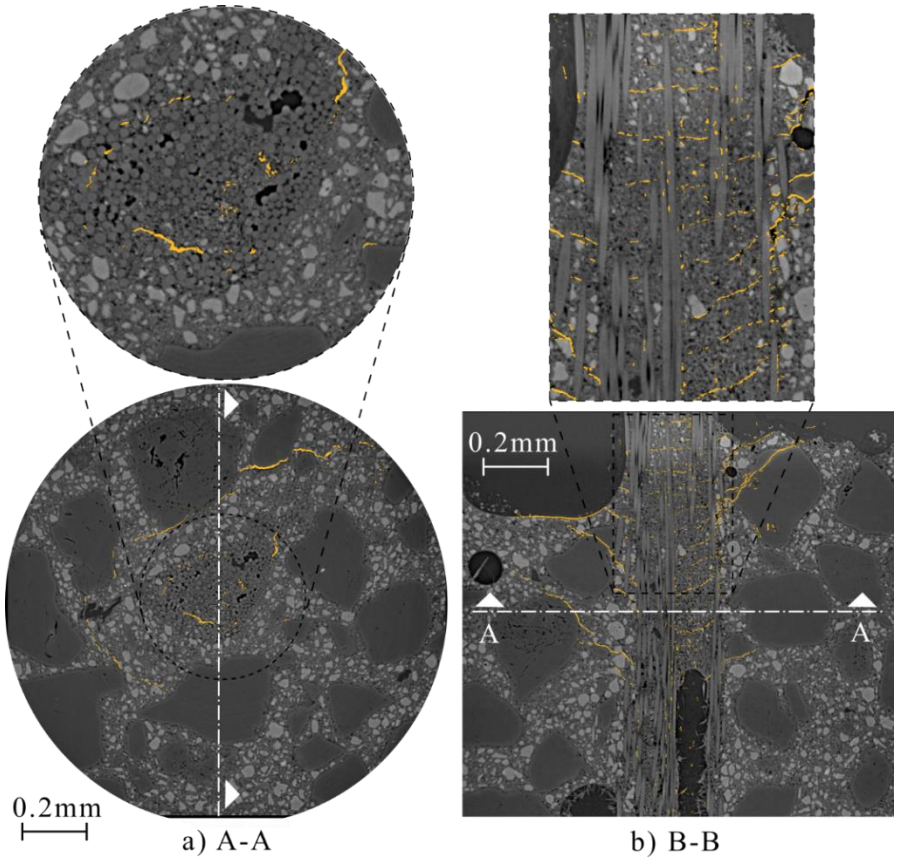

Figure 13: Transversal and longitudinal slices of crack+transformed image at the upper end of BF+NAV (sd1) specimen at a force level of 34 N (dashed lines on both slices indicate the section plane used to draw the other slice).

4.4 Other composite systems with single-fibre yarn

This subsection discusses the use of the proposed methodology when a smooth single-fibre steel yarn is used as reinforcement for mortar. The study of such simpler case would be of great interest to better understand interface behaviour as this specific situation involves a simplified geometry, which would allow one to use simpler models. Unfortunately, observations of tests on SSF based specimens were not conclusive because of numerous practical difficulties.

Qualitative observations do not reveal any crack emitted in the matrix or any other proof showing that interfacial damage occurs. Nevertheless, the force-elongation tension stiffening curve plotted on left graph in Figure 2 shows, for both SSF specimens, a strong decrease in the stiffness of the overall system with the increasing of the loading. When put together, these observations suggest that decohesion between yarn and matrix is likely to take place in the vicinity of the yarn. Unfortunately, this location is also subject to a strong edge artefact due to the large X-ray absorption contrast between steel and mortar. This artefact is revealed by subtracting the overlap areas of two successive images in the reference state, i.e. with an intact interface. The image subtractions of different loading states, i.e. with presumed debonded interface, show similar features and therefore do not allow detecting other features than this artefact. Moreover, as the single-fibre yarn is smooth and does not show enough internal grey-level contrast, no measurement of local displacement discontinuity between yarn and mortar was possible using DVC. The use of another material for the single-fibre yarn, which would show enough internal contrast and a lower difference of absorption with the mortar, would ensure the image processing to be run much more efficiently. This is left for further investigations.

4.5 Analysis of crack orientations in different specimens.

Previous observations show that cracks orientation is very sensitive to microstructure heterogeneity. Consequently, the observation of one single crack does not permit to characterise the representative geometry of all interfacial cracks. Therefore, a statistical analysis of crack orientation is provided in Figure 14, which shows the statistical distributions of the two angles presented in section 3.5 (Figure 7) for the three studied specimens. The angle θ_d (Figure 14 top left) is the angle between the crack normal transversal component and radial direction $\boldsymbol{e_r}$, while the angle φ (Figure 14 top right) is the one between crack normal and yarn direction. Considering that cracks are mostly conical, θ_d distribution then represents the roundness of the crack cone (a Dirac distribution located at zero would then be the distribution for a circular transversal profile) and φ distribution represents the slope of the crack plane with the transversal plane.

Based on the assumption of conical cracks, it is possible to quantify in average the geometrical characteristics of the cracks from their orientation map $\boldsymbol{n}(\boldsymbol{X})$. Such analysis results in a more visual representation of the crack geometry than the orientation histograms and can provide overall typical patterns related to interfacial properties. To that end, we propose two simplified descriptions of crack geometries by considering separately the mean transversal section of cracks $r(\theta)$, obtained by averaging over all distances to the yarn, and the mean axisymmetric profile $z(r)$, obtained by averaging over all polar angles (Figure 14 bottom). The details of the calculation are available in the appendix.

Regarding the roundness of the crack cones, the SGF+NAG3 specimen exhibits the most round one among all mean transversal cross-sections $r(\theta)$, i.e. corresponds to the slightly narrowest distribution of θ_d. Complementarily, comparing mean transversal profiles with shape and

orientation of yarn cross-section confirms the influence of the yarn cross-section shape and orientation on the crack transversal profiles. This effect was previously observed qualitatively on some transversal tomography slices. Regarding the inclination of the crack cones, the distribution on the angle φ and the axisymmetric profile $z(r)$ both suggest it is mostly controlled by the matrix properties.

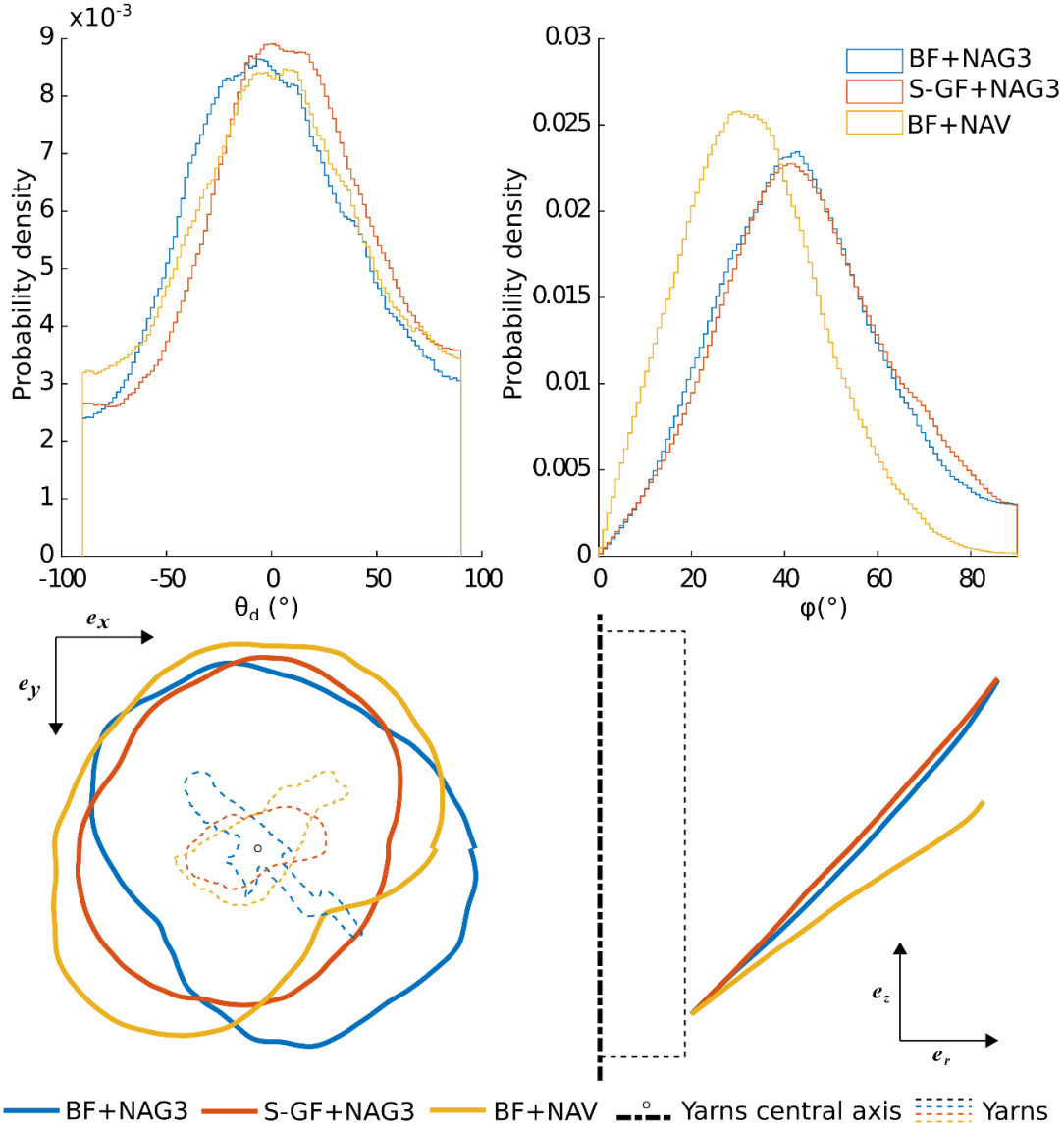

Figure 14: Top: Angular distribution of normal vector of crack plane with respect to yarn direction: angle θ_d at the left and angle φ at the right (see fig.7); Bottom left: mean transversal cross-section of cracks $r(\theta)$ normalized to an arbitrary size; Bottom right: mean longitudinal crack profile $z(r)$ at the right-bottom corner. In these plots, position and cross-section of yarns are recalled in dotted lines.

This simplified geometrical modelling is useful to obtain first quantitative information on the crack shape to compare globally the damage features of the various systems. It would be imprecise when the crack transverse cross section are not sufficiently round or when they evolve with the distance to the yarn. A more accurate averaged geometrical description of the evolution of crack normal vector orientation as a coupled problem $\boldsymbol{n}(r,\theta,z)$, albeit more complex, would be an interesting perspective of the present analysis.

5 CONCLUSIONS / PERSPECTIVES

A specific in situ tension stiffening test was conducted at the Anatomix beamline of Synchrotron Soleil. It allows, with non-destructive observation of the damage typology, for studying its link with the materials microstructure, and its evolution with increasing loading. The testing frame was designed using fast prototyping techniques to adapt it to the microtomography setup of Anatomix. Several increasing monitored levels of force were applied to six different specimens, and local X-ray computed tomography imaging was performed at each level, covering efficiently the whole interfacial area, with submicrometric voxel size. From these raw 3D images, despite possible tracking of the larger cracks, detection of tiny cracks is very difficult due to the strongly heterogeneous microstructure of the mortar. To enhance cracking detection, a specific method based on DVC, image subtraction technique and hessian-based segmentation was used. This technique permits to enhance the identification of tiny cracks with a subvoxel aperture around 0.1µm, by removing similar information between reference and loaded images. It keeps only changes between both states such as tiny cracks. To further distinguish cracks from imaging artefacts, the crackness image is computed from the hessian of grey level of subtracted images. Moreover, the crack orientation map is also calculated for voxels belonging to a crack. This methodology is shown to be an efficient tool to characterise interfacial debonding damage typology and geometry for multi-fibre yarn in a cementitious matrix. Different damage typologies have been identified depending on the type of composite system. They are gathered in Table 3 and their mean geometries have been described quantitatively from the local orientation of cracks.

In most multi-fibre yarn systems, the cracks are shaped as cones emitted from the fibre and developing in the matrix towards the sample tip. The transverse shape of the cones is very similar to the transverse shape of the yarn. The angle of the cones is observed to depend on the type of mortar. This type of damage, similar to cracking patterns that appear at rebar ribs in reinforced concrete demonstrates the great interfacial strength between yarn and matrix. This great interfacial strength is also highlighted by the dense transversal multi-cracking that occurs in matrix located between separate groups of fibres. The second type of interface damage is a local splitting between yarn and matrix that indicates a smaller local interfacial bond. Mixed situations have also been identified. The present study highlights the influence of the yarn cross-section shape on the interfacial bond between multi-fibre yarn and cementitious matrix, characterised by the damage mode type.

A straightforward perspective would be to use the presented methodology to study other multi-fibres structure, such as multi ends roving and different impregnation systems [20]**.** The methodology would also provide interesting quantitative data for calibrating micromechanical models and thus permit to optimise the yarn choice depending on a particular matrix in a particular process. Finally, the experimental methodology could be performed on specimens with several parallel yarns close to each other to specifically study transversal multi-cracking damage patterns and the reciprocal influence between yarns.

ACKNOWLEDGEMENT

The work presented in this article is part of a PhD project supported by Labex MMCD (MultiScale Modelling and Experimentation of Materials for Sustainable Construction), which benefits from French government grants managed by the French National Research Agency ANR within the frame of the national program *Investments for the Future* (grant no. ANR-11-LABX-022-01). ANATOMIX is an Equipment of Excellence (EQUIPEX) also funded by the *Investments for the Future* program, project *NanoimagesX*, grant no. ANR-11-EQPX-0031. The authors want to express their gratitude to Marine Lemaire for the design of the acquisition electronics and the programming of the dedicated LabView application, and to Dr Sébastien Brisard for his helpful presence during image acquisition at Synchrotron Soleil.

APPENDIX

This appendix details the determination of the simplified representative geometry of the cracks. According to section 4.5, we suppose that the cracks are mostly conical and that their representative geometries can be defined by two uncoupled descriptions: the transversal cross-section of cracks $r(\theta)$ and the mean axisymmetric profile $z(r)$.

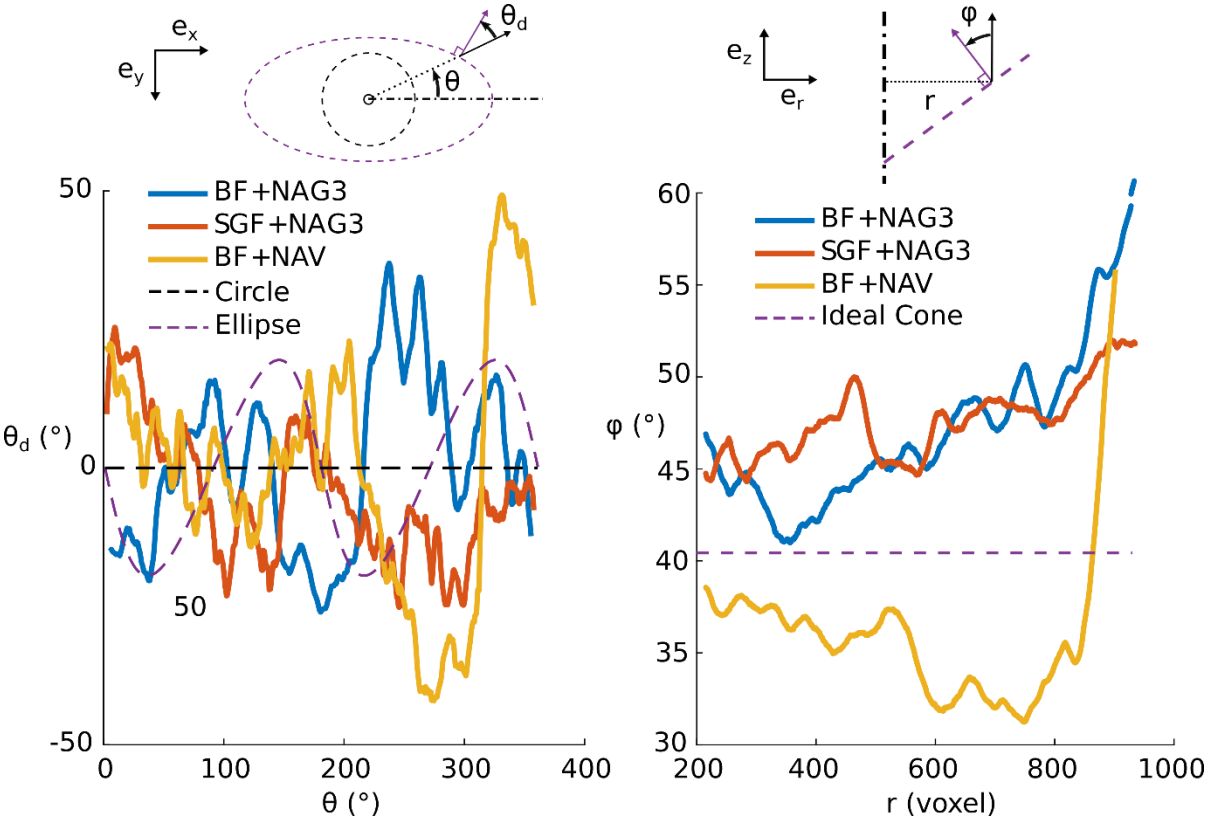

Figure 15: Evolution of average crack transversal angle θ_d with respect to polar angle θ and average axisymmetric angle φ with respect to distance to fibre r. Theoretical examples are superimposed to measured data to illustrate the analysis.

On one hand, the transversal section of cracks $r(\theta)$ is supposed to be independent of r and z apart from a homothety. Then, it can be obtained from the evolution of θ_d with respect to θ,

given by the orientation map, by integration of $\frac{dr}{r\,d\theta} = \tan(\theta_d(\theta))$. The function $\theta_d(\theta)$ is obtained by averaging the data of the orientation maps over all detected cracks.

On the other hand, the axisymmetric profile $z(r)$ is the same for all cracks apart from a translation, and does not depend on θ. We also consider that $\boldsymbol{n}$ belongs to $\{\boldsymbol{e_r}, \boldsymbol{e_z}\}$. Consequently, it yields $\frac{dz}{dr} = \tan(\varphi(r))$. It can then be computed from the evolution of φ with respect to r, given by the orientation map. The function $\varphi(r)$ is again obtained by averaging the data of the orientation maps over all detected cracks. Distances smaller than $r < 200$ voxels are here rejected because they may correspond to locations in the fibre.

Despite the important fluctuations in the orientation map, the great amount of data permits to perform a moving average. A sampling procedure provides a 0.5 voxel discretization for both $\theta_d(\theta)$ and $\varphi(r)$. These sampled evolutions are both plotted in Figure 15. Numerical integrations are then performed to obtain the respective transversal and axisymmetric profiles, plotted at the bottom of Figure 14.

BIBLIOGRAPHY

[1] A. Nanni, *Journal of Structural Engineering* **1993**, *119*, 3344.
[2] O. Chaallal, B. Benmokrane, *Composites Part B: Engineering* **1996**, *27*, 245.
[3] P.L. Walton, A.J. Majumdar, *Composites* **1975**, *6*, 209.
[4] P. Jun, V. Mechtcherine, *Cement and Concrete Composites* **2010**, *32*, 810.
[5] Z. Salari, B. Vakhshouri, S. Nejadi, *Journal of Building Engineering* **2018**, *20*, 264.
[6] U. Häußler-Combe, J. Hartig, *Cement and Concrete Composites* **2007**, *29*, 279.
[7] J. Hegger, S. Voss, *Engineering Structures* **2008**, *30*, 2050.
[8] L.A.S. Kouris, T.C. Triantafillou, *Construction and Building Materials* **2018**, *188*, 1221.
[9] L. Ascione, G. de Felice, S. De Santis, *Composites Part B: Engineering* **2015**, *78*, 497.
[10] M. Konrad, R. Chudoba, *Acta Polytechnica* **2004**, *44*, 8.
[11] H.L. Cox, *British Journal of Applied Physics* **1952**, *3*, 72.
[12] R.C. deVekey, A.J. Majumdar, *Magazine of Concrete Research* **1968**, *20*, 229.
[13] P. Lawrence, *Journal of Materials Science* **1972**, *7*, 1.
[14] V. Laws, *Composites* **1982**, *13*, 145.
[15] H. Stang, Z. Li, S.P. Shah, *Journal of Engineering Mechanics* **1990**, *116*, 2136.
[16] X.B. Zhang, H. Aljewifi, J. Li, *Construction and Building Materials* **2013**, *47*, 456.
[17] S. Zhandarov, E. Pisanova, E. Mäder, *Composite Interfaces* **2000**, *7*, 149.
[18] F. Teklal, A. Djebbar, S. Allaoui, G. Hivet, Y. Joliff, B. Kacimi, *Composite Structures* **2018**, *201*, 791.
[19] H. Aljewifi, X.B. Zhang, J. Li, in *2014 International Conference on Composite Materials & Renewable Energy Applications (ICCMREA)*, IEEE, Sousse, Tunisia **2014**, 1.
[20] H. Aljewifi, *Etude du comportement mécanique à l'arrachement de fils multi-filamentaires enrobés dans une matrice cimentaire et influence de l'imprégnation*, UNIVERSITE DE CERGY-PONTOISE, **2011**.
[21] A. Enfedaque, D. Cendón, F. Gálvez, V. Sánchez-Gálvez, *Construction and Building Materials* **2010**, *24*, 1302.
[22] P. Purnell, N.R. Short, C.L. Page, A.J. Majumdar, *Cement and Concrete Research* **2000**, *30*, 1747.

[23] N. Ducoulombier, C. Chateau, M. Bornert, J.-F. Caron, T. Weitkamp, J. Perrin, in *10th International Conference on Fracture Mechanics of Concrete and Concrete Structures (FraMCoS-X)*, G. Pijaudier-Cabot, P. Grassl And C. La Borderie, Bayonne, France **2019**.
[24] Y. Goto, *Journal of the American Concrete Institute* **1971**, *68*, 244.
[25] E. Maire, T. Morgeneyer, C. Landron, J. Adrien, L. Helfen, *Comptes Rendus Physique* **2012**, *13*, 328.
[26] B.K. Bay, T.S. Smith, D.P. Fyhrie, M. Saad, *Experimental Mechanics* **1999**, *39*, 217.
[27] C. Chateau, T.T. Nguyen, M. Bornert, J. Yvonnet, *Strain* **2018**, *54*, e12276.
[28] M. Voorn, U. Exner, A. Rath, *Computers & Geosciences* **2013**, *57*, 44.
[29] T. Weitkamp, M. Scheel, J. Giorgetta, V. Joyet, V. Le Roux, G. Cauchon, T. Moreno, F. Polack, A. Thompson, J. Samama, *Journal of Physics: Conference Series* **2017**, *849*, 012037.
[30] N. Leclercq, J. Bisou, F. Blache, F. Langlois, S. Lê, K. Medjoubi, C. Mocuta, S. Poirier, *Proceedings of the 15th Int. Conf. on Accelerator and Large Experimental Physics Control Systems* **2015**, *ICALEPCS2015*, Australia.
[31] D. Paganin, S.C. Mayo, T.E. Gureyev, P.R. Miller, S.W. Wilkins, *Journal of Microscopy* **2002**, *206*, 33.
[32] A. Mirone, E. Brun, E. Gouillart, P. Tafforeau, J. Kieffer, *Nuclear Instruments and Methods in Physics Research Section B: Beam Interactions with Materials and Atoms* **2014**, *324*, 41.
[33] A. King, N. Guignot, P. Zerbino, E. Boulard, K. Desjardins, M. Bordessoule, N. Leclerq, S. Le, G. Renaud, M. Cerato, M. Bornert, N. Lenoir, S. Delzon, J.-P. Perrillat, Y. Legodec, J.-P. Itié, *Review of Scientific Instruments* **2016**, *87*, 093704.
[34] M. Bornert, J.-M. Chaix, P. Doumalin, J.-C. Dupre, T. Fournel, D. Jeulin, E. Maire, M. Moreaud, H. Moulinec, *Instrumentation, Mesure, Métrologie* **2004**, *4*, 43.
[35] H. Schreier, J.-J. Orteu, M.A. Sutton, *Image Correlation for Shape, Motion and Deformation Measurements*, Springer US, Boston, MA **2009**.
[36] J.-Y. Buffiere, E. Maire, *Imagerie 3D En Mécanique Des Matériaux*, Hermes/Lavoisier**2014**.
[37] M. Bornert, F. Brémand, P. Doumalin, J.-C. Dupré, M. Fazzini, M. Grédiac, F. Hild, S. Mistou, J. Molimard, J.-J. Orteu, L. Robert, Y. Surrel, P. Vacher, B. Wattrisse, *Experimental Mechanics* **2009**, *49*, 353.
[38] F. Hild, S. Roux, *Strain* **2006**, *42*, 69.
[39] Y. Chen, L. Gélébart, C. Chateau, M. Bornert, A. King, P. Aimedieu, C. Sauder, *Experimental Mechanics* **2020**, *60*, 409.
[40] C. Chateau, L. Gélébart, M. Bornert, J. Crépin, D. Caldemaison, C. Sauder, *Journal of the Mechanics and Physics of Solids* **2014**, *63*, 298.